

Simulating Electronic Structure on Bosonic Quantum Computers

Rishab Dutta, Nam P. Vu, Chuzhi Xu, Delmar G. A. Cabral, Ningyi Lyu, Alexander V. Soudackov, Xiaohan Dan, Haote Li, Chen Wang, and Victor S. Batista*

Cite This: *J. Chem. Theory Comput.* 2025, 21, 2281–2300

Read Online

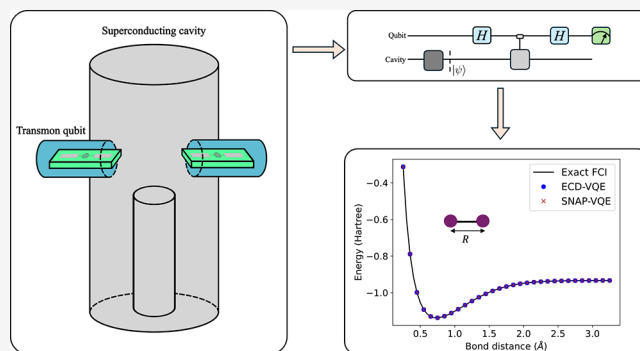
ACCESS |

Metrics & More

Article Recommendations

Supporting Information

ABSTRACT: Quantum harmonic oscillators, or qumodes, provide a promising and versatile framework for quantum computing. Unlike qubits, which are limited to two discrete levels, qumodes have an infinite-dimensional Hilbert space, making them well-suited for a wide range of quantum simulations. In this work, we focus on the molecular electronic structure problem. We propose an approach to map the electronic Hamiltonian into a qumode bosonic problem that can be solved on bosonic quantum devices using the variational quantum eigensolver (VQE). Our approach is demonstrated through the computation of ground potential energy surfaces for benchmark model systems, including H_2 and the linear H_4 molecule. The preparation of trial qumode states and the computation of expectation values leverage universal ansatzes based on the echoed conditional displacement (ECD), or the selective number-dependent arbitrary phase (SNAP) operations. These techniques are compatible with circuit quantum electrodynamics (cQED) platforms, where microwave resonators coupled to superconducting transmon qubits can offer an efficient hardware realization. This work establishes a new pathway for simulating many-fermion systems, highlighting the potential of hybrid qubit-qumode quantum devices in advancing quantum computational chemistry.



1. INTRODUCTION

Understanding the ground and excited states of many-fermion systems is one of the fundamental problems in chemistry and physics. Accurate simulation of molecular electronic structure, a many-fermion problem, is critical in understanding chemical reaction mechanisms or designing new molecules and materials with novel properties. Classical computers are fundamentally restricted in simulating exact molecular electronic structure problems beyond a certain system size,¹ and approximate classical computing methods fail to simulate a range of electronic structure systems with strong electron correlation.² The recent interest in developing algorithms based on quantum computers can potentially address this issue.

The current era of noisy intermediate scale quantum (NISQ) computers relies on the quantum information unit known as qubits which are two-level quantum systems. NISQ computers have inherent limitations due to the decoherence associated with qubits and the quantum operators acting on them. Nevertheless, several hybrid quantum-classical algorithms have been developed to simulate molecular electronic structure, that combine resources from both classical and quantum devices.^{3–8} One of the steps in all these algorithms involves mapping the fermionic Hamiltonian of the molecule of interest to a qubit Hamiltonian.^{9,10}

The development of bosonic quantum devices introduces a fundamentally novel approach to quantum computing. Bosonic

quantum computing can be conceptually understood as computations with quantum harmonic oscillators (QHOs), also known as *qumodes*, instead of qubits. Qumodes can store quantum information in the unbounded Hilbert space of QHOs and naturally support continuous variable bases due to the position and momentum operators associated with oscillator modes. A range of applications has been demonstrated using bosonic quantum devices for chemistry,¹¹ including simulation of molecular vibronic spectra,^{12–14} understanding conical intersections,¹⁵ and implementing quantum dynamics for modeling chemical processes.^{16,17}

Qumodes can be realized with different hardware approaches,¹⁸ including but not limited to electromagnetic fields inside resonators,^{19,20} and the motion of trapped ions.^{21,22} A promising and rapidly evolving hardware platform for realizing bosonic quantum computation is the circuit quantum electrodynamics (cQED) approach.^{23–26} The cQED hardware comprises microwave resonators as the qumodes and superconducting qubits based on Josephson junctions acting as

Received: October 17, 2024

Revised: February 10, 2025

Accepted: February 12, 2025

Published: March 3, 2025



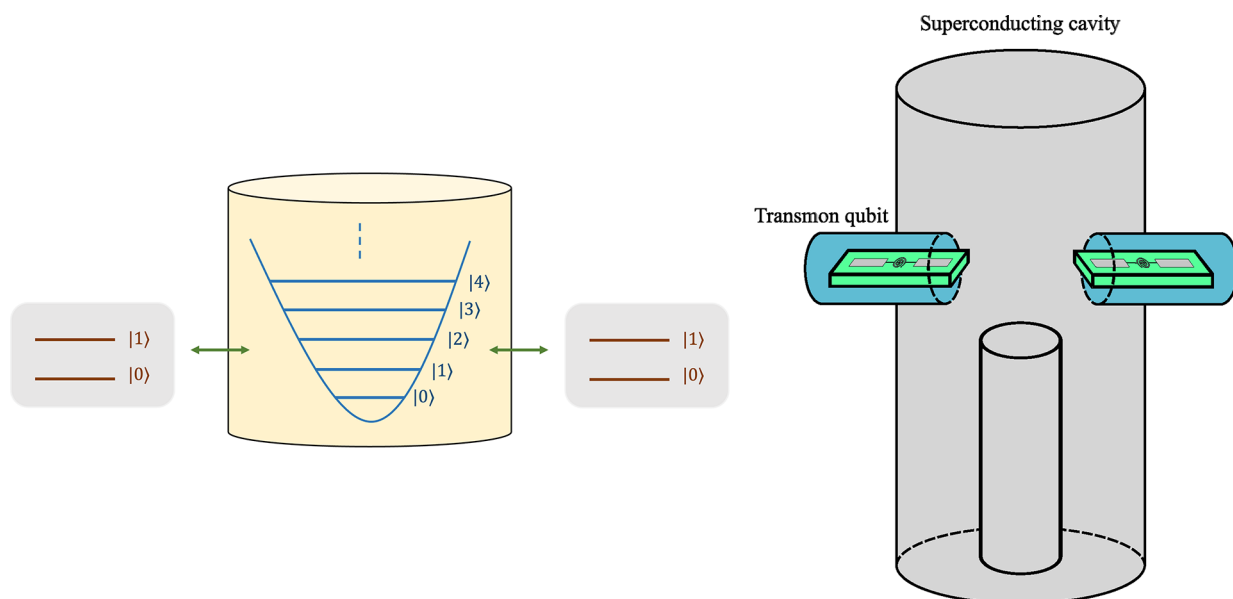


Figure 1. Illustration of a quantum device consisting of one qumode and two qubits. (Left) A conceptual illustration of a qumode coupled with two qubits. (Right) A schematic of the quantum hardware where two transmon qubits are connected to a microwave resonator that acts as the qumode in the cQED approach.

the nonlinear element that controls and measures the quantum information. Bosonic cQED devices with 3D resonator geometries can have a photon lifetime of up to two seconds.²⁷ Conceptually, the cQED devices are a hybrid qubit-qumode hardware approach that promises a new quantum computing paradigm.²⁵

Quantum algorithms for molecular electronic structure tailored for qubits, however, can not be trivially applied to qumode hardware due to the fundamental difference between qubits which are spin-1/2 systems, and qumodes which are bosonic. An important step in simulating molecular electronic structure on bosonic quantum computers would be to map the corresponding fermionic Hamiltonian to a bosonic one. There has been substantial past work on fermion to boson mapping, including exact and approximate transformations.^{28–36} An exact state mapping between fermionic Slater determinants and bosonic Fock states of QHOs was established by Ohta based on the fact that particle-hole excitations from the Fermi vacuum can be represented as photon transitions.³⁷ An exact operator mapping between a number-conserving bilinear fermionic operator and oscillator projection operators can be derived from this state mapping, as shown by Dhar, Mandal, and Suryanarayana,³⁸ which we will call the *direct* mapping. Although the direct mapping is conceptually appealing, it may lead to an impractical number of bosonic operator terms in the mapped Hamiltonian for larger electronic systems.

In this work, we introduce a *qubit-assisted* fermion to boson mapping, where the fermionic operators will be first mapped to qubit operators followed by a qubit to qumode mapping. We will show how the direct and qubit-assisted fermion to boson mappings can be applied to transform the molecular electronic structure Hamiltonian to a system of qumodes. To the best of our knowledge, this is the first time a molecular electronic structure Hamiltonian has been simulated as a bosonic system, which allows us to develop bosonic variational quantum eigensolver (VQE) algorithms for finding the ground state of the molecular electronic system using trial states generated by a qubit-qumode device. Specifically, the bosonic VQE methods

can take advantage of the unique universal gate sets native to the hybrid qubit-qumode device, such as the echoed conditional displacement (ECD) gates combined with qubit rotations or the selective number-dependent arbitrary phase (SNAP) combined with qumode displacement gates. We apply the resulting ECD-VQE and SNAP-VQE approaches to show that the expectation value of a Hamiltonian of four qubits representing the electronic structure of the dihydrogen molecule can be computed using quantum hardware consisting of two transmon qubits and one microwave resonator acting as a qumode, as illustrated in Figure 1, while the trial energy is optimized on a classical computer. We also generalize our approach for larger systems where many qubits can be mapped to a few qumodes with the operations modularized and optimized for hardware efficiency. We illustrate our multi-qumode generalization on the ground state of the linear H₄ molecule to exemplify how our proposed method can outperform traditional qubit-based variational approaches. Although this work focuses specifically on the molecular electronic structure Hamiltonian, the techniques presented here can be applied to any many-qubit and many-fermion Hamiltonians such as systems studied in condensed matter³⁹ or nuclear physics.²⁸

2. BACKGROUND

The electronic Hamiltonian under the Born–Oppenheimer approximation can be represented in the second quantization form as^{40,41}

$$H_{\text{elec}} = \sum_{pq} h_q^p f_p^\dagger f_q + \frac{1}{2} \sum_{pqrs} v_{rs}^{pq} f_p^\dagger f_q^\dagger f_r f_s \quad (1)$$

where p, q, r, s indices represent molecular spin-orbitals $\{\chi_p\}$ and $\{f_p^\dagger, f_q\}$ are the corresponding fermionic creation and annihilation operators, respectively. The scalars $\{h_q^p\}$ and $\{v_{rs}^{pq}\}$ are the one-electron and the two-electron integrals,

$$h_q^p = \int d\mathbf{x} \chi_p^*(\mathbf{x}) \left(-\frac{1}{2} \nabla^2 - \sum_A \frac{Z_A}{r_A} \right) \chi_q(\mathbf{x}) \quad (2a)$$

$$v_{rs}^{pq} = \frac{\int d\mathbf{x}_1 d\mathbf{x}_2 \chi_p^*(\mathbf{x}_1) \chi_q^*(\mathbf{x}_2) \chi_r(\mathbf{x}_2) \chi_s(\mathbf{x}_1)}{r_{12}} \quad (2b)$$

where ∇ is the Laplacian operator representing differentiation with respect to the coordinates of each electron, Z_A is the nuclear charge of the A^{th} nucleus, $r_A = |\mathbf{r} - \mathbf{R}_A|$ is the distance between an electron and A^{th} nucleus, $r_{12} = |\mathbf{r}_1 - \mathbf{r}_2|$ is the distance between two electrons. These elementary fermionic operators follow the canonical anticommutation relation (CAR)

$$\{f_p^\dagger, f_q^\dagger\} = f_p^\dagger f_q^\dagger + f_q^\dagger f_p^\dagger = 0 \quad (3a)$$

$$\{f_p, f_q\} = f_p f_q + f_q f_p = \delta_{pq} \quad (3b)$$

where the fermionic mode indices span the M number of spin-orbital functions $\{\chi_p\}$. The Pauli exclusion principle is then equivalent to the relation $(f_p^\dagger)^2 = 0$, which is simply a consequence of the CAR in eq (3).

We assume the number of spin-orbitals M to be an even integer since there is an underlying $M/2$ number of spatial functions $\{\phi_p(\mathbf{r})\}$ which can associate with either up-spin $\alpha(\omega)$ or down-spin $\beta(\omega)$ functions. Thus, N electrons in M molecular spin-orbitals give rise to $\binom{M}{N}$ number of many-electron basis states, each of which is an antisymmetrized product state called the Slater determinants, defined as

$$|p_1, \dots, p_N\rangle_F \equiv f_{p_1}^\dagger \dots f_{p_N}^\dagger |-\rangle_F \quad (4)$$

where $|-\rangle_F$ is the physical vacuum representing the state with $N = 0$ electrons and any $f_p |-\rangle_F = 0$. We provide further context to the electronic structure problem within the [Supporting Information](#). We note that the combinatorial number of many-electrons basis states scales exponentially with the problem size and thus proves challenging to enumerate and perform operations on. This is where quantum computer promises to be useful, as it can potentially address the problem of finding stationary states and energies at a reduced computational cost.

3. QUBIT-QUMODE CIRCUITS

It is possible to transform the electronic Hamiltonian of eq 1 to a bosonic Hamiltonian with an algebraic map of $E_q^p = f_p^\dagger f_q$ operators to bosonic operators based on its Fock basis. However, it may not be an efficient approach for mapping systems with a large number of electrons. We present this direct mapping in [Appendix A](#). In this section, we focus on a more systematic approach to transform the electronic Hamiltonian in terms of a linear combination of qubit-qumode operators, with the help of a fermion to qubit mapping. We discuss this qubit-assisted mapping for the rest of this article.

3.1. Fermion to qubit mapping. Let us review the basic concepts related to qubits which are two-level quantum systems. The elementary one-qubit operators are the Pauli matrices

$$X = \begin{pmatrix} 0 & 1 \\ 1 & 0 \end{pmatrix}, \quad Y = \begin{pmatrix} 0 & -i \\ i & 0 \end{pmatrix}, \quad Z = \begin{pmatrix} 1 & 0 \\ 0 & -1 \end{pmatrix} \quad (5)$$

which can be generalized to multi-qubit operators by taking tensor products of Pauli matrices (also known as a Pauli word), e.g., $X_1 Y_2 Z_3 = X \otimes Y \otimes Z$ represents a three-qubit operator. We will also use $\{\sigma_j\}$ to denote Pauli matrices where $j \in \{x, y, z\}$ represent X, Y and Z matrices. Any qubit Hamiltonian can be represented as a linear combination of Pauli words

$$H_Q = \sum_{\mu=1}^{N_H} (g_\mu \otimes_{p=1}^{N_Q} \sigma_p) = \sum_{\mu=1}^{N_H} g_\mu \mathbb{P}_\mu^{(N_Q)} \quad (6)$$

where $\{g_\mu\}$ are scalar Hamiltonian coefficients and N_Q is the number of qubits. The number of terms N_H is usually a computationally manageable integer for a physical Hamiltonian.

The molecular electronic Hamiltonian of eq 1 can be transformed to a qubit Hamiltonian of the form in eq 6 by applying a fermion to qubit mapping. There are many fermion to qubit maps that have been explored recently. For example, the Jordan–Wigner transformation (JWT)⁴² maps the fermionic creation and annihilation operators to the following Pauli words

$$f_p^\dagger \rightarrow \frac{1}{2}(X_p - iY_p) \otimes_{q<p} Z_q \quad (7a)$$

$$f_p \rightarrow \frac{1}{2}(X_p + iY_p) \otimes_{q<p} Z_q \quad (7b)$$

where the qubit indices represent the spin-orbital indices of the fermionic operators. This means H_{elec} is transformed by JWT to a qubit Hamiltonian of eq 6 with $N_H = O(M^4)$ and $N_Q = M$, where M is the number of spin orbitals. We will focus on JWT in this paper, but we note that recent developments on fermion to qubit maps that go beyond JWT can reduce the scaling of both N_H and N_Q in terms of the number of spin orbitals.^{43,44}

3.2. Qubit to Qumode Mapping. Usually, some of the g_j coefficients for different $\mathbb{P}_j^{(N_Q)}$ operators in eq 6 may be the same, in which case these operators can be grouped and H_{elec} can be written as

$$H_Q = \sum_{\mu=1}^{N'_H} g_\mu W_\mu^{(N_Q)} \quad (8)$$

where $\{W_\mu^{(N_Q)}\}$ are either a single or a summation of N_Q -qubit Pauli words and $N'_H < N_H$. Each $W_\mu^{(N_Q)}$ operator can be represented in the computational basis by a matrix of dimensions $2^{N_Q} \times 2^{N_Q}$. We want to map the multi-qubit $W_\mu^{(N_Q)}$ operator to a parametrized qumode operator with the help of an ancilla qubit, as implementable in a cQED transmon-resonator device. Since the target multi-qubit operator can be arbitrary, the implemented qumode operator must be represented by a set of universal qubit-qumode gates.

There are different universal qubit-qumode gates that have been explored in the past.^{45–50} We focus here on a qubit-qumode universal unitary circuit $U_A^{(N_d)}$ based on N_d unitary blocks of the following form^{45,46,49}

$$U_A^{(N_d)}(\boldsymbol{\theta}^G, \boldsymbol{\theta}^G, \boldsymbol{\varphi}^G) = U_{ER}(\beta_{N_d}^G, \theta_{N_d}^G, \varphi_{N_d}^G) \dots U_{ER}(\beta_1^G, \theta_1^G, \varphi_1^G) \quad (9a)$$

$$U_{ER}(\beta, \theta, \varphi) = ECD(\beta)[R(\theta, \varphi) \otimes \mathbb{1}] \quad (9b)$$

where the symbols “A” and “G” represent the ansatz unitary and the parameters for the target unitary gates, respectively. We will denote N_d as the circuit depth of the universal ansatz from now on. Each unitary gate U_{ER} , schematically represented in Figure 2 consists of a qubit rotation

$$R(\theta, \varphi) = \exp[-i(\theta/2)(\cos \varphi X + \sin \varphi Y)] \quad (10)$$

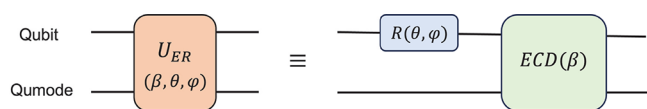


Figure 2. Qubit-qumode gate consisting of one qubit rotation as defined in eq 10 and an ECD gate as defined in eq 11.

and an echoed conditional displacement (ECD) operator

$$ECD(\beta) = |1\rangle\langle 0| \otimes D(\beta/2) + |0\rangle\langle 1| \otimes D(-\beta/2) \quad (11)$$

with the displacement operator defined as

$$D(\beta) = \exp(\beta \hat{b}^\dagger - \beta^* \hat{b}) \quad (12)$$

where \hat{b}^\dagger and \hat{b} are the bosonic creation and annihilation operators. We refer the reader to Appendix C for more details on the ECD with qubit rotation ansatz.

Before discussing further, let us first formalize a general multi-qubit to qubit-qumode mapping approach. Let us assume we have a target operator W_T corresponding to N_Q qubits, which means it can be also understood as a qumode operator with Fock cutoff $L = 2^{N_Q}$. There is no constraint on the W_T except that it is a quantum operation, i.e., W_T can be non-unitary. We want to find a parametrized qubit-qumode operator V such that the following is true

$$(\mathbb{1}_2 \otimes W_T)|0\rangle_Q \otimes |\psi\rangle_R \approx V|0\rangle_Q \otimes |\psi\rangle_R \quad (13)$$

where “Q” and “R” represent the states of the qubit and resonator and $|\psi\rangle$ is an arbitrary qumode state. We have fixed the qubit state to $|0\rangle$ since our mapping is focused only on the qumode space. This also allows us to optimize in the $|0\rangle_Q$ subspace of the full Hilbert space spanned by the combined qubit-qumode basis states, thus making the numerical optimization for finding the parameters more robust, as discussed below. We express the qubit-qumode operator V as a linear combination of ECD and rotation operators

$$V(\lambda, \beta^G, \theta^G, \varphi^G) = \sum_{j=1}^{N_t} \lambda_j U_j^{(N_d)}(\beta_j^G, \theta_j^G, \varphi_j^G) \quad (14a)$$

$$U_j^{(N_d)}(\beta_j^G, \theta_j^G, \varphi_j^G) = U_{ER}(\beta_{j,N_d}^G, \theta_{j,N_d}^G, \varphi_{j,N_d}^G) \cdots U_{ER}(\beta_{j,1}^G, \theta_{j,1}^G, \varphi_{j,1}^G) \quad (14b)$$

where N_d is the depth of each unitary gate and N_t is the number of terms in the linear expansion. We have to solve the following optimization problem to find the parameters for a given target matrix W_T

$$\min_{\lambda, \beta^G, \theta^G, \varphi^G} F = \frac{1}{L^2} \sum_{n,m=0}^{L-1} |\langle 0, n | (\mathbb{1}_2 \otimes W_T) | 0, m \rangle - \langle 0, n | V(\lambda, \beta^G, \theta^G, \varphi^G) | 0, m \rangle|^2 \quad (15)$$

where $|0, n\rangle \equiv |0\rangle_Q \otimes |n\rangle_R$ and $\{|n\rangle\}$ are the qumode Fock basis states. The Fock cutoff $L = 2^{N_Q}$ is the dimension of the target N_Q -qubit operator W_T . In the context of mapping the Hamiltonian in eq 8 into a qubit-qumode system, each of the $W_j^{(N_Q)}$ represents the W_T operator in eq 15. The qubit Hamiltonian in eq 8 can then be approximated as

$$H_Q \approx \sum_{\mu=1}^{N_H'} g_\mu \sum_{j=1}^{N_t} \lambda_{\mu,j} U_{\mu,j}^{(N_d)}(\beta_{\mu,j}^G, \theta_{\mu,j}^G, \varphi_{\mu,j}^G) \quad (16)$$

where the parameters for the ECD and rotation gates can be represented by the tensors $\beta^G, \theta^G, \varphi^G$. After the optimization of eq 15 is achieved, these tensors may be stored in the memory and can be reused for further calculations involving H_Q .

3.3. Computation of Expectation Values. Our goal is to find the ground state energy of the Hamiltonian H_Q by variationally updating a normalized trial state $|\psi\rangle$ while we compute the trial energy

$$\min_{\psi} E(\psi) = \frac{\langle \psi | H_Q | \psi \rangle}{\langle \psi | \psi \rangle} = \langle \psi | H_Q | \psi \rangle \quad (17)$$

with the help of a quantum device, following the variational quantum eigensolver (VQE) approach.³ Since the mapped Hamiltonian in eq 16 can now be understood as a Hamiltonian of one qumode, we explore the space of qumode states $\{|\psi\rangle\}$ as the trial state. Then the trial qumode states $|\psi\rangle$ can be generated from a universal qubit-qumode gate involving ECD and qubit rotations. In other words, we prepare a parametrized qubit-qumode state

$$|\Psi\rangle = U_A^{(D)}(|0\rangle_Q \otimes |0\rangle_R) \quad (18)$$

where the unitary is written as

$$U_A^{(D)}(\beta^W, \theta^W, \varphi^W) = U_{ER}(\beta_D^W, \theta_D^W, \varphi_D^W) \cdots U_{ER}(\beta_1^W, \theta_1^W, \varphi_1^W) \quad (19a)$$

$$U_{ER}(\beta, \theta, \varphi) = ECD(\beta)[\mathbb{1} \otimes R(\theta, \varphi)] \quad (19b)$$

and D is the circuit depth of the ansatz unitary circuit for the trial state preparation. The qumode state $|\psi\rangle$ can be projected from the qubit-qumode state $|\Psi\rangle$ by measuring the qubit part and continuing with qumode circuit if the qubit measurement results in state $|0\rangle$. In other words, the disentangled qubit-qumode state can be represented as

$$|0\rangle_Q \otimes |\psi\rangle_R = \frac{P_0 |\Psi\rangle}{\langle \Psi | P_0 | \Psi \rangle} \quad (20)$$

where $P_0 = |0\rangle\langle 0| \otimes \mathbb{1}$ and $|\Psi\rangle$ is defined in eq 18. We note that bosonic ansatz has also been recently explored for molecular electronic structure in ref 51.

The expectation value of H_Q for a trial state $|\psi\rangle$ can now be written as

$$\begin{aligned} \langle \psi | H_Q | \psi \rangle &\approx \sum_{\mu=1}^{N_H'} g_\mu \sum_{j=1}^{N_t} \lambda_{\mu,j} \text{Re}(\langle \psi | U_{\mu,j}^{(N_d)}(\beta_{\mu,j}^G, \theta_{\mu,j}^G, \varphi_{\mu,j}^G) | \psi \rangle) \\ &= \sum_{\mu=1}^{N_H'} g_\mu \sum_{j=1}^{N_t} \lambda_{\mu,j} M_{\mu,j} \end{aligned} \quad (21)$$

where $\{M_{\mu,j}\}$ can be computed by a Hadamard test involving another ancilla qubit. The controlled unitary in the Hadamard test includes two types of gates: Qubit-controlled qubit rotation and qubit-controlled ECD gate. The latter is two-

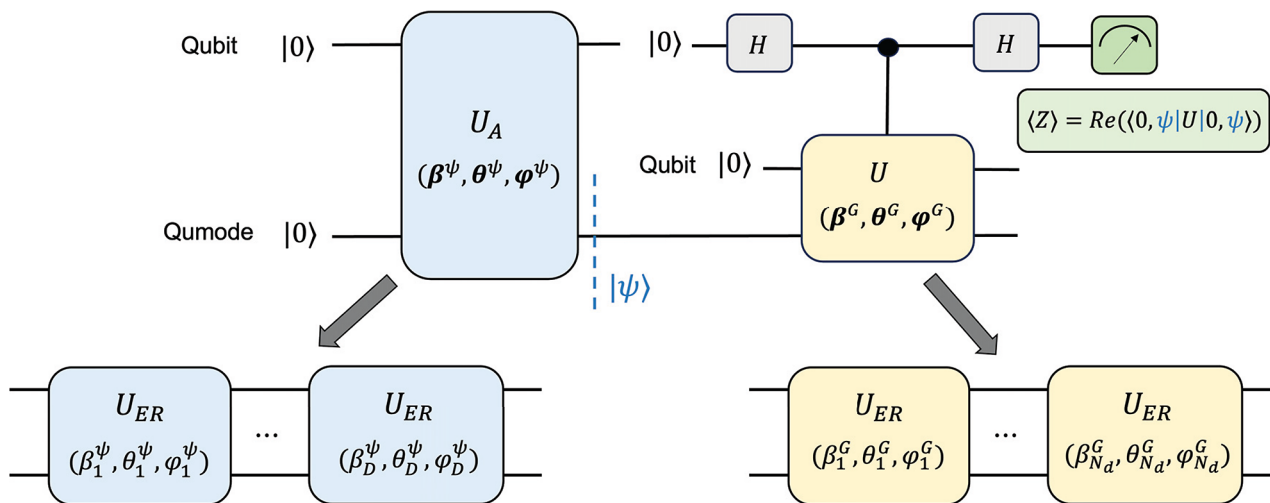


Figure 3. Full circuit involving one qumode with two qubits for computing the expectation value of a qubit-qumode unitary U for a qumode state $|\psi\rangle$, where the U_{ER} operation is defined in Figure 2. After generating a qumode state $|\psi\rangle$, the Hadamard test computes $\text{Re}(\langle 0, \psi | U | 0, \psi \rangle)$. The controlled-ECD gates can be decomposed further in terms of CNOT and conditional displacement gates, as discussed in Appendix E.1 and Figure 19.

qubit one-qumode gate and can be decomposed in terms of two-qubit and qubit-qumode gates, as discussed in Appendix E.1. The full circuit for the generation of the trial state and computation of expectation values involving one qumode and two qubits is illustrated in Figure 3. The two summations in eq 21 can be efficiently computed on a classical device after getting the set of $\{M_{\mu,j}\}$ from quantum device measurements. We name this approach to optimize eq 17 with ECD-rotation circuits as ECD-VQE.

It should be noted that for some specific electronic structure systems, the *global* ground state of the mapped qubit Hamiltonian H_Q may not have the desired electron number of the system of interest since after mapping the fermion to qubit mapping, the Hilbert space of qubits contains all of the fermion number sectors. In that case, explicit particle number constraint can be imposed by modifying the cost function⁵²

$$\min_{\psi, \lambda} C_N = \langle \psi | H_Q | \psi \rangle + \lambda [\langle \psi | (\hat{N} - N) | \psi \rangle]^2 \quad (22)$$

where λ is a Lagrange multiplier, N is the number of electrons and $\hat{N} = \sum_{p=1}^M f_p^\dagger f_p$ is the fermionic total number operator, which can be mapped to the following qubit operator

$$\hat{N} \rightarrow \sum_{p=1}^M \frac{1}{2} (\mathbb{I}_p + Z_p) \quad (23)$$

using the Jordan-Wigner transformation. The expectation value $\langle \psi | \hat{N} | \psi \rangle$ can be computed following the discussion above for computing $\langle \psi | H_Q | \psi \rangle$. This constrained cost function approach of eq 22 can also be applicable to spin-symmetries by mapping the fermionic \hat{S}_F^2 to its corresponding qubit operator \hat{S}_Q^2 and optimizing the cost function below⁵²

$$\min_{\psi, \lambda} C_S = \langle \psi | H_Q | \psi \rangle + \lambda [\langle \psi | \hat{S}_Q^2 | \psi \rangle - S(S+1)]^2 \quad (24)$$

where S is the total spin quantum number. However, optimization of eq 17 is sufficient for many electronic systems, including the dihydrogen molecule discussed here, which we discuss below.

3.4. Ground State Energy of the Dihydrogen Molecule. As a specific example, we apply the ideas discussed above to simulate the electronic structure of the H_2 molecule in a minimal basis in this section.⁴⁰ We choose one spatial function per hydrogen atom, which leads to the following molecular spatial orbitals

$$\phi_g = \mathcal{N}_g (1s_1 + 1s_2) \quad (25a)$$

$$\phi_u = \mathcal{N}_u (1s_1 - 1s_2) \quad (25b)$$

where \mathcal{N}_g and \mathcal{N}_u are the normalization factors based on the spatial functions chosen, and one popular choice is the STO-3G minimal basis⁵³ that approximates the Slater-type atomic functions with three real-valued Gaussian functions.⁴⁰ Having two spatial orbitals means we have an electronic system of two electrons in four spin-orbitals, as shown by the molecular orbital diagram in Figure 4. Let us define the four spin-orbitals as

$$|\chi_0\rangle \equiv |\phi_g, \alpha\rangle, \quad |\chi_1\rangle \equiv |\phi_g, \beta\rangle \quad (26a)$$

$$|\chi_2\rangle \equiv |\phi_u, \alpha\rangle, \quad |\chi_3\rangle \equiv |\phi_u, \beta\rangle \quad (26b)$$

where α and β denote spin-orbitals with up and down electron spins, respectively.

The electronic structure Hamiltonian of the dihydrogen molecule in a minimal basis can be written as⁹

$$\begin{aligned} H_F = & h_{\text{nuc}} + h_{00}^0 f_0^\dagger f_0 + h_{11}^1 f_1^\dagger f_1 + h_{22}^2 f_2^\dagger f_2 + h_{33}^3 f_3^\dagger f_3 + v_{10}^{01} f_0^\dagger f_1^\dagger f_1 f_0 \\ & + v_{32}^{23} f_2^\dagger f_3^\dagger f_3 f_2 + v_{30}^{03} f_3^\dagger f_0^\dagger f_0 f_3 + v_{21}^{12} f_1^\dagger f_2^\dagger f_2 f_1 + (v_{20}^{02} - v_{02}^{20}) f_0^\dagger f_2^\dagger f_2 f_0 \\ & + (v_{31}^{13} - v_{13}^{31}) f_1^\dagger f_3^\dagger f_3 f_1 + v_{12}^{21} v_{03}^{30} f_0^\dagger f_1^\dagger f_2 f_3 + \text{h.c.} + v_{32}^{23} (f_0^\dagger f_1^\dagger f_3 f_2 + \text{h.c.}) \end{aligned} \quad (27)$$

which can then be expressed as the following four-qubit Hamiltonian using JWT⁹

$$\begin{aligned} H_F \rightarrow H_Q = & g_1 + g_2(Z_0 + Z_1) + g_3(Z_2 + Z_3) + g_4 Z_0 Z_1 \\ & + g_5(Z_0 Z_2 + Z_1 Z_3) + g_6(Z_0 Z_3 + Z_1 Z_2) + g_7 Z_2 Z_3 \\ & + g_8(X_0 Y_1 Y_2 X_3 + Y_0 X_1 X_2 Y_3 - X_0 X_1 Y_2 Y_3 - Y_0 Y_1 X_2 X_3), \end{aligned} \quad (28)$$

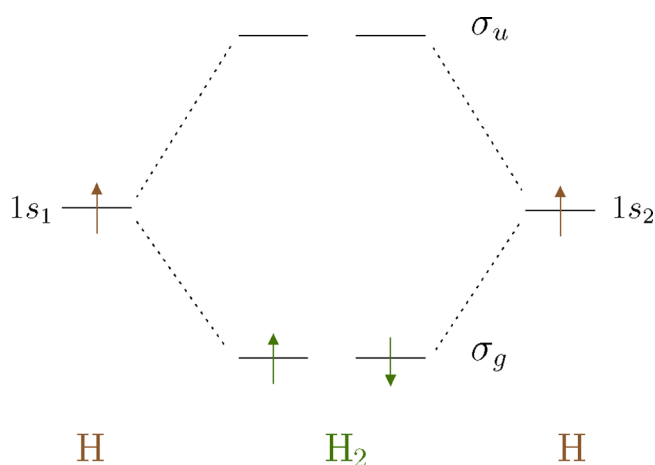


Figure 4. A molecular orbital diagram corresponding to the H_2 molecule in a minimal basis. The molecular orbitals, σ_g and σ_u , are built from $1s$ atomic orbitals of the two hydrogen atoms. In second quantization, the diagram represents the Slater determinant $|0,1\rangle_F = f_0^\dagger f_1^\dagger |-\rangle_F$, where the first and second spin-orbitals share the σ_g spatial function.

where the scalars $\{g_j\}$ are defined in Table 1 and tensor product is assumed. For example, the term $Z_1 Z_3$ represents the four-qubit operator $\mathbb{1} \otimes Z \otimes \mathbb{1} \otimes Z$, and so on. Following eq 8, we can also represent eq 28 as

$$H_Q = g_1 + \sum_{\mu=2}^8 g_\mu W_\mu^{(4)} \quad (29)$$

where $W_2^{(4)} = Z_0 + Z_1$, $W_3^{(4)} = Z_2 + Z_3$, and so on. We have observed that after the optimization is achieved based on the loss function defined in eq 15, we can expand eq 29 as

$$H_Q \approx g_1 + \sum_{\mu=2}^8 g_\mu \sum_{j=1}^{15} \lambda_{\mu,j} U_{\mu,j}^{(10)}(\beta_{\mu,j}^G, \theta_{\mu,j}^G, \varphi_{\mu,j}^G) \quad (30)$$

where each of the $W_\mu^{(4)}$ operator is written as linear combination of $N_i = 15$ ECD-rotation unitaries, each with circuit depth $N_d = 10$. The converged loss function for each of

the $W_\mu^{(4)}$ operators is shown in Table 2, where the Broyden–Fletcher–Goldfarb–Shanno (BFGS) method was used as the

Table 2. Converged Losses for the Hamiltonian Operator Terms Corresponding to Equation 29 Following the Optimization of the Loss Function Defined in Equation 15^a

Operator	Converged Loss
$W_2^{(4)}$	5×10^{-12}
$W_3^{(4)}$	3×10^{-11}
$W_4^{(4)}$	5×10^{-12}
$W_5^{(4)}$	2×10^{-11}
$W_6^{(4)}$	1×10^{-11}
$W_7^{(4)}$	1×10^{-11}
$W_8^{(4)}$	2×10^{-12}

^aThe results are for a linear combination of $N_i = 15$ unitaries, each of depth $N_d = 10$.

optimizer as implemented in SciPy.⁵⁴ The expectation value of H_Q for a qumode state generated by the ECD-rotation ansatz can now be computed by following the discussions in Section 3.3 and Figure 3.

Computation of expectation values allowed the emulation of VQE for the dihydrogen molecule on a classical computer, where the ECD-VQE optimization as defined in eq 17 has been achieved using the BFGS method. As shown in Figure 5, the ECD-rotation ansatz circuit with a depth $D = 9$ accurately reproduces the ground state energies of the dihydrogen molecule in the STO-3G basis, where the exact ground state energies in this basis can be found by diagonalizing the Hamiltonian, also known as full configuration interaction (FCI). All calculations were done using QuTip⁵⁵ and OpenFermion.⁵⁶ We compare the approximate trial energies computed using the decomposed Hamiltonian defined by eq 30 with the exact trial energies in Figure 6. The energy errors in Figure 6 show that it is possible that the approximate energies can sometimes go below the exact energies. However, these negative errors are numerically tolerable since the error ranges are far smaller than the chemical accuracy regime.

Table 1. Definition of Scalars in Equation 28 Using Nuclear Repulsion and One-Electron and Two-Electron Integral Terms

Coefficient	Definition
g_1	$h_{\text{nuc}} + \frac{1}{2}(h_0^0 + h_1^1 + h_2^2 + h_3^3) + \frac{1}{4}[v_{10}^{01} + v_{32}^{23} + v_{30}^{03} + v_{21}^{12} + (v_{20}^{02} - v_{02}^{02}) + (v_{31}^{13} - v_{13}^{13})]$
g_2	$-\frac{1}{2}h_0^0 - \frac{1}{4}[v_{10}^{01} + v_{30}^{03} + (v_{20}^{02} - v_{02}^{02})]$
g_3	$-\frac{1}{2}h_2^2 - \frac{1}{4}[v_{32}^{23} + v_{21}^{12} + (v_{20}^{02} - v_{02}^{02})]$
g_4	$\frac{1}{4}v_{10}^{01}$
g_5	$\frac{1}{4}(v_{20}^{02} - v_{02}^{02})$
g_6	$\frac{1}{4}v_{30}^{03}$
g_7	$\frac{1}{4}v_{32}^{23}$
g_8	$\frac{1}{4}v_{12}^{03}$

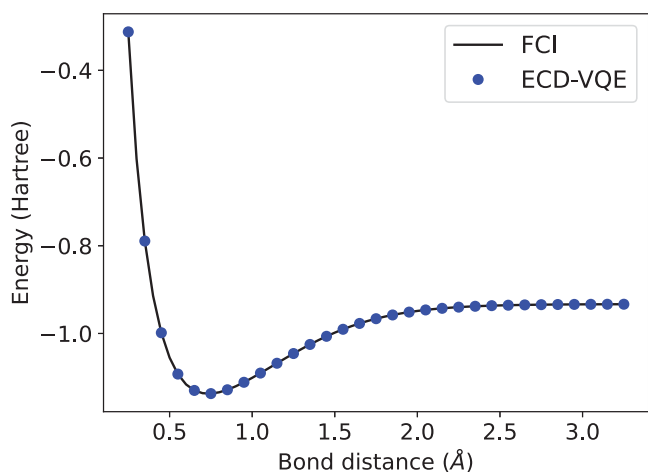


Figure 5. Comparison of dihydrogen molecule ground state energies in STO-3G minimal basis using the ECD-VQE approach as discussed in Section 3 with the FCI energies. The ECD with qubit rotation ansatz circuit for the trial state preparation has a depth of $D = 9$.

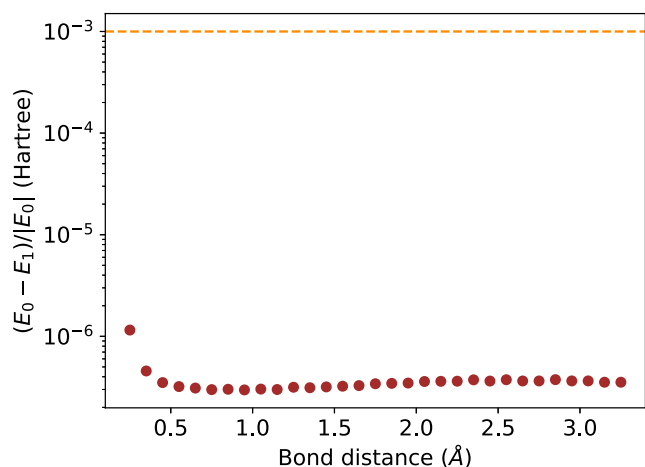


Figure 6. Accuracy in energies computed using the linear decomposition involving ECD with qubit rotation unitaries. Here, E_0 represents the energy computed with the original qubit Hamiltonian defined in eq 28, whereas E_1 represents energy computed with its decomposition defined in eq 30. The qumode states for the expectation values are taken from the converged trial states corresponding to the ECD-VQE calculations shown in Figure 5.

4. QUMODE MAPPING WITHOUT ANCILLA QUBIT

Another universal bosonic unitary can be implemented by repeating blocks of the following parametrized gate^{47,50}

$$U_{SD}(\alpha, \theta) = S(\theta)D(\alpha) \quad (31)$$

where $D(\alpha)$ is the displacement gate and $S(\theta)$ is the selective number-dependent arbitrary phase (SNAP) gate⁵⁷

$$S(\theta) = \sum_{n=0}^{L-1} e^{i\theta}|n\rangle\langle n| \quad (32)$$

where $|n\rangle\langle n|$ is the Fock basis projection operator and L is the Fock cutoff for the qumode. We illustrate the SNAP-displacement gate in Figure 7 and discuss more details on this gate set including its universality for a single qumode in Appendix D. Since the parametrization of the SNAP gate already includes a complex phase, the displacement coefficient in eq 31 can be assumed to be real-valued.

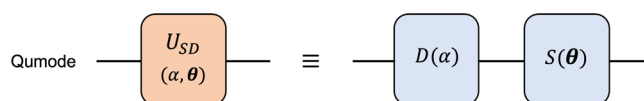


Figure 7. Qumode gate consisting of one displacement gate as defined in eq 12 and a SNAP gate as defined in eq 32.

Following Section 3.2, we can now approximate an arbitrary target unitary operator V_T with our parametrized unitary

$$U^{(N_d)}(\alpha^G, \theta^G) = U_{SD}(\alpha_{N_d}, \theta_{N_d}) \cdots U_{SD}(\alpha_1, \theta_1) \quad (33)$$

where N_d is the circuit depth. The corresponding optimization problem to find the parameters for a given target unitary V_T now becomes

$$\min_{\alpha^G, \theta^G} F = \frac{1}{L^2} \sum_{n,m=0}^{L-1} |\langle n|V_T|m\rangle - \langle n|U^{(N_d)}(\alpha^G, \theta^G)|m\rangle|^2 \quad (34)$$

where $\{|n\rangle\}$ are the qumode Fock basis states and the Fock cutoff L is given by the dimension of V_T . We note that even though we can understand the parametrized unitary ansatz in eq 33 as a sequence of qumode gates conceptually, the hardware implementation of these gates do require an ancilla qubit, as discussed in Appendix D.

4.1. Dihydrogen Molecule. We now apply this to the qubit Hamiltonian for the dihydrogen molecule in a minimal basis, as defined in eq 28. We have observed that it is possible to accurately approximate each of the Pauli words of the Hamiltonian in eq 28 with SNAP-displacement circuit of depth $N_d = 16$, as shown in Table 3. Thus, we can write the electronic structure Hamiltonian of the dihydrogen molecule as

$$H_Q \approx g_1 + \sum_{j=1}^{14} v_j U_j^{(16)}(\alpha_j^G, \theta_j^G) \quad (35)$$

where the coefficients $\{v_j\}$ can be easily deduced from eq 28.

Table 3. Converged Losses for the Four-Qubit Pauli Words Corresponding to Equation 28 Following the Optimization of the Loss Function Defined in Equation 34^a

Operator	Converged Loss	Operator	Converged Loss
$Z \otimes \mathbb{1} \otimes \mathbb{1} \otimes \mathbb{1}$	8×10^{-14}	$\mathbb{1} \otimes Z \otimes Z \otimes \mathbb{1}$	5×10^{-14}
$\mathbb{1} \otimes Z \otimes \mathbb{1} \otimes \mathbb{1}$	1×10^{-13}	$\mathbb{1} \otimes Z \otimes \mathbb{1} \otimes Z$	2×10^{-13}
$\mathbb{1} \otimes \mathbb{1} \otimes Z \otimes \mathbb{1}$	3×10^{-14}	$\mathbb{1} \otimes \mathbb{1} \otimes Z \otimes Z$	3×10^{-14}
$\mathbb{1} \otimes \mathbb{1} \otimes \mathbb{1} \otimes Z$	9×10^{-14}	$X \otimes Y \otimes Y \otimes X$	5×10^{-14}
$Z \otimes Z \otimes \mathbb{1} \otimes \mathbb{1}$	8×10^{-15}	$Y \otimes X \otimes X \otimes Y$	1×10^{-13}
$Z \otimes \mathbb{1} \otimes Z \otimes \mathbb{1}$	3×10^{-14}	$X \otimes X \otimes Y \otimes Y$	1×10^{-13}
$Z \otimes \mathbb{1} \otimes \mathbb{1} \otimes Z$	4×10^{-14}	$Y \otimes Y \otimes X \otimes X$	6×10^{-14}

^aThe results are for the SNAP-displacement circuit as the parameterized circuit with depth $N_d = 16$.

The computation of expectation value $\langle \psi | H_Q | \psi \rangle$ for a trial qumode state $|\psi\rangle$ can be achieved by a little modification of the circuit described in Section 3.3 and Figure 3. A major improvement of the SNAP-displacement approach over the ECD with qubit rotation approach can be understood by comparing Eq. 30 and Eq. 35. Specifically, the Hadamard test of only 14 unitaries are needed in the case of SNAP-displacement approach compared to 120 unitaries in the case of ECD with qubit rotation for computing the trial energy of

the dihydrogen molecule. We illustrate the full circuit for the SNAP-displacement approach in Figure 8, where the qumode

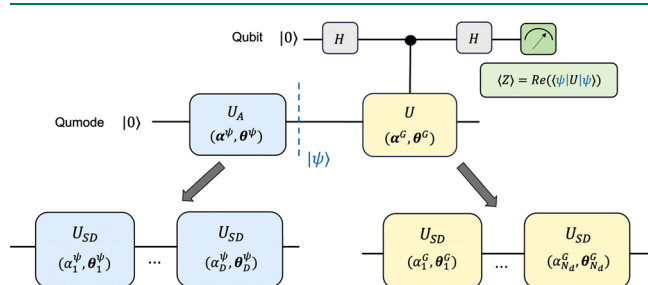


Figure 8. Full circuit involving one qumode with one qubit for computing the expectation value of a qubit-qumode unitary U for a qumode state $|\psi\rangle$. After generating a qumode state $|\psi\rangle$, the Hadamard test computes $\text{Re}(\langle\psi|U|\psi\rangle)$.

trial ansatz $|\psi\rangle = U_A^{(D)}|0\rangle$ is also parametrized with a SNAP-displacement circuit ansatz

$$U_A^{(D)}(\alpha^\psi, \theta^\psi) = U_{SD}(\alpha_D^\psi, \theta_D^\psi) \cdots U_{SD}(\alpha_1^\psi, \theta_1^\psi) \quad (36)$$

where D is the trial ansatz circuit depth and U_{SD} is defined in Eq. 31. We name this approach to optimize Eq. 17 with SNAP-displacement circuits as SNAP-VQE. As mentioned above, the auxiliary qubit for implementing the SNAP gate may be omitted in circuits conceptually. For the controlled SNAP-displacement ansatz, the two-qubit one-qumode controlled-SNAP gates can be implemented by combining two-qubit CNOT with qubit-qumode SNAP gates following Eq. 84, as illustrated in Figure 9. It should be noted that since the qumode state preparation is separate from the expectation value computation part in Figure 8, it can also be achieved with an ECD with qubit rotation ansatz or any other universal bosonic circuits in principle.

We compare the ECD-VQE and SNAP-VQE approaches for the dihydrogen molecule on a classical computer in Figure 5, where the BFGS method has been applied for the classical optimization part as defined in Eq. 17. All calculations were done using QuTip and OpenFermion. The ECD-rotation ansatz circuit has a depth of $D = 9$ whereas the SNAP-displacement ansatz circuit has a depth of $D = 4$ for the trial state preparation part. It is clear from the right panel of Figure 10 that the SNAP-VQE is a better approach in terms of accuracy and circuit depth, although both the methods achieve energetic error well below the chemical accuracy regime. Overall, we have observed that the SNAP-displacement ansatz has greater variational flexibility than the ECD-rotation ansatz, thus can represent unitary circuits more compactly for both Pauli words and as a trial state. This is justified by more

tunability of the SNAP parameters that can precisely affect each of the Fock basis states. An important distinction between ECD and SNAP gates is that the ECD can be implemented in the weakly dispersive regime between the qubit and qumode,⁴⁵ where a strong dispersive interaction is currently needed for implementing the latter.⁴⁷ We refer the readers to Appendix E.2 for more details on the comparison of the hardware implementation of ECD and SNAP gates.

4.2. Generalization to Multiple Qumodes. The SNAP-VQE approach allows a single unitary circuit with practical depth for computing expectation values using a Hadamard test. This allows the development of a modular approach to generalize the SNAP-VQE approach for an arbitrary number of qubits after mapping them to a few qumodes. We discuss how to extend the SNAP-VQE approach for multiple qumodes and the quantum hardware necessary to implement multimode trial states here.

In principle, N_Q qubits can be mapped to the unitary gates of a single qumode with a Fock cutoff of $L = 2^{N_Q}$. In practice, it is more appropriate to partition the tensor product space of N_Q qubits, which still has the advantage of replacing many qubits with a few qumodes, while having more control over the hardware. Let us assume we want to map N_Q qubits to N_R ($< N_Q$) qumodes with corresponding Fock cutoffs given by $\{L_1, \dots, L_{N_R}\}$. The N_Q -qubit Hamiltonian in Eq. 6 can then be represented as

$$H_Q = \sum_{\mu=1}^{N_H} g_\mu \mathbb{P}_\mu^{(N_{Q,1})} \otimes \cdots \otimes \mathbb{P}_\mu^{(N_{Q,N_R})} \rightarrow \sum_{\mu=1}^{N_H} g_\mu \mathcal{U}_\mu^{(1)} \otimes \cdots \otimes \mathcal{U}_\mu^{(N_R)} \quad (37)$$

where $\mathbb{P}_\mu^{(N_{Q,j})}$ is a Pauli word of $N_{Q,j}$ qubits, $N_Q = N_{Q,1} + \cdots + N_{Q,N_R}$, and $\mathcal{U}_\mu^{(j)}$ is a SNAP-displacement ansatz with a Fock cutoff $L_j = 2^{N_{Q,j}}$. Let us also assume that any $N_{Q,j} \leq 4$, which means the Fock cutoff for each qumode can not be more than 16, consistent with the current qumode hardware capabilities.¹³ This gives us the blueprint to generalize SNAP-VQE to a qubit Hamiltonian with an arbitrary number of qubits, as mentioned below.

- The optimization problem of Eq. 34 is solved for all possible Pauli words of up to 4 qubits. This classical optimization involves matrices up to 16×16 dimensions. The optimal parameters are then stored as a library.
- Any qubit Hamiltonian H_Q with N_Q number of qubits is partitioned into subsystems, each containing no more than 4 qubits.
- The mapping of Eq. 37 is known based on the parameter library mentioned above, and a maximum of 4-fold

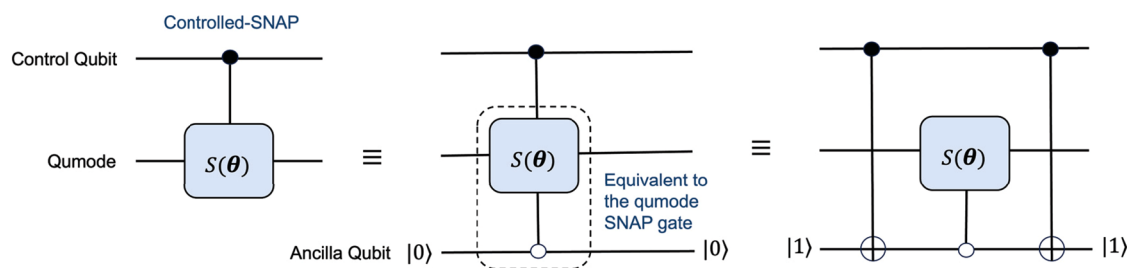


Figure 9. Implementation of controlled-SNAP gate with the ancilla qubit dispersively coupled to the qumode explicitly shown. The circuit is based on the fact the SNAP gate implementation needs the ancilla qubit to be returned to $|0\rangle$ state after the operation, as defined in Eq. 84.

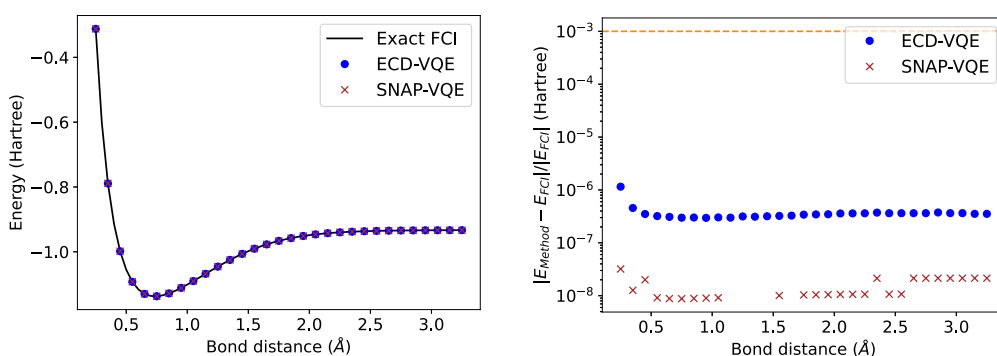


Figure 10. Comparison of dihydrogen molecule ground state energies in STO-3G minimal basis using ECD-VQE and SNAP-VQE approaches, as discussed in Section 3 and Section 4, respectively. The ECD with qubit rotation ansatz circuit has a depth of $D = 9$ and the SNAP with displacement ansatz circuit has a depth of $D = 4$ for the trial state preparation parts. The orange horizontal line in the right panel represents the minimum energy error needed for chemical accuracy, usually in the milliHartree range.

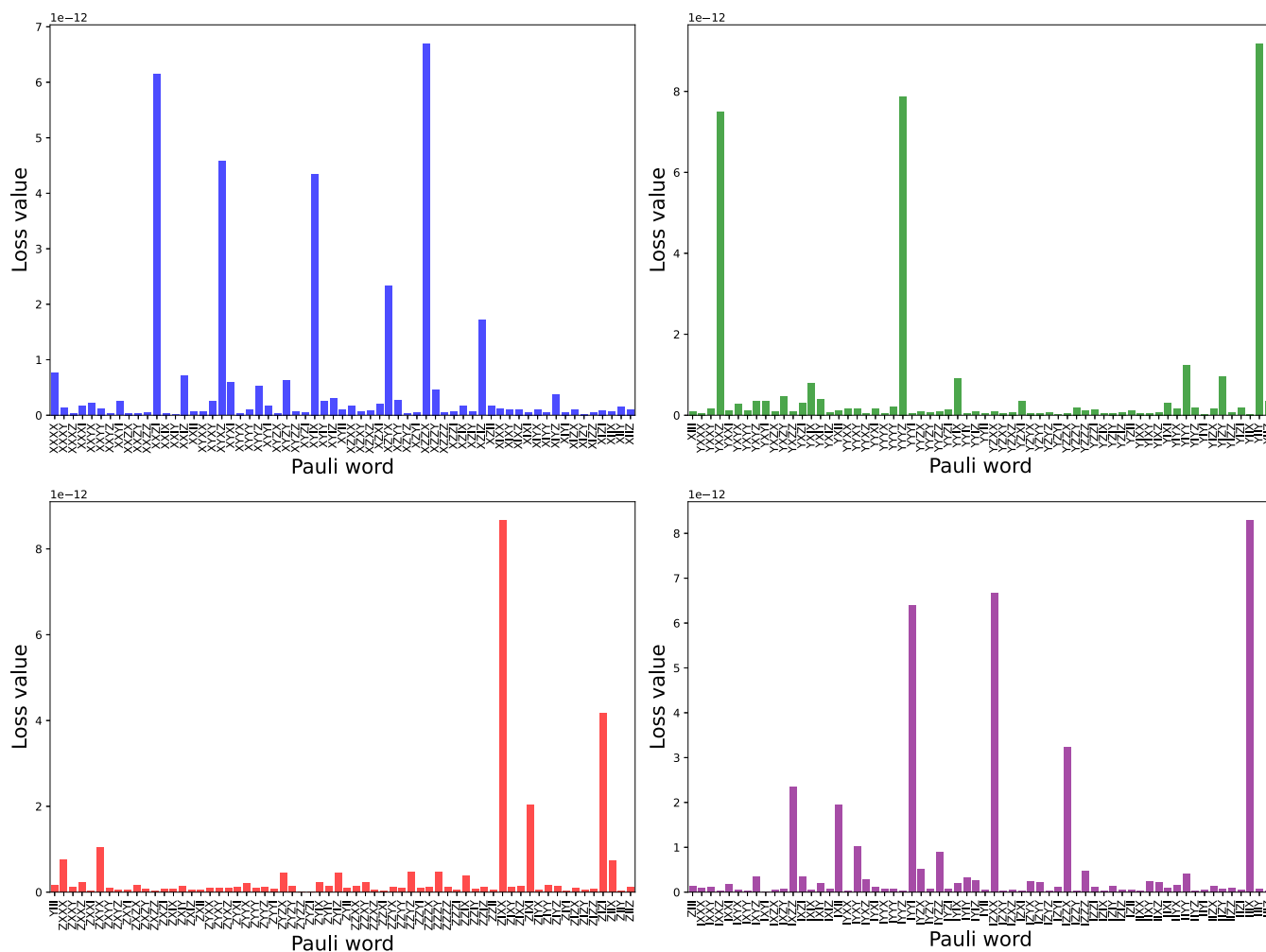


Figure 11. Converged losses for all possible non-trivial Pauli words based on the optimization defined in Eq. 34. The results are for the SNAP-displacement universal circuit ansatz with depth $N_d = 16$.

resource reduction can be achieved in terms of the qubit to qumode mapping.

We show the optimal loss function values defined in Eq. 34 for all possible four-qubit Pauli words in Figure 11. It is clear from Figure 11 that all the converged values are at least less than 10^{-11} , which represents the error bound for the Hamiltonian mapping.

The Hamiltonian mapping to multiple qumodes discussed above also allows us to generalize the circuit from the one qumode scenario for computing the expectation value to the multimode case. The hardware needed involves one transmon qubit connected to multiple qumodes.⁴⁸ Given a multi-qumode trial state $|\psi\rangle$, we can compute the expectation value using a Hadamard test approach

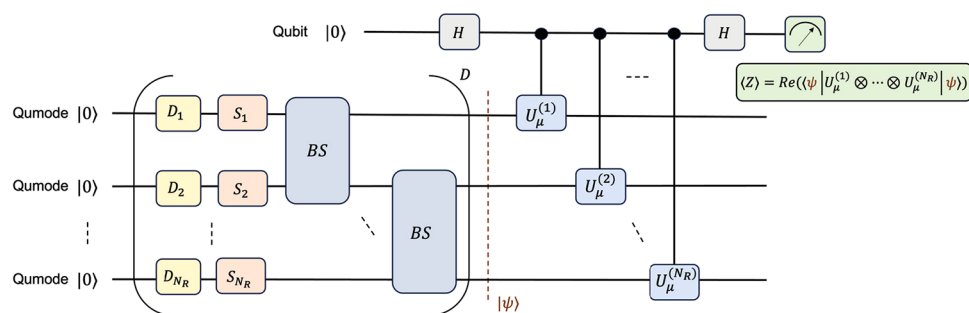


Figure 12. Full circuit involving multiple qumodes with one qubit for computing the expectation value as defined in Eq. 38 based on the trial state defined in eq (40). The circuit contains an additional ancilla qubit not shown here which is coupled to all qumodes.

$$\langle \psi | H_Q | \psi \rangle = \sum_{\mu=1}^{N_H} g_\mu \langle \psi | \mathcal{U}_\mu^{(1)} \otimes \dots \otimes \mathcal{U}_\mu^{(N_R)} | \psi \rangle \quad (38)$$

using a sequence of qubit-controlled SNAP displacement unitaries $\{\mathcal{U}_\mu\}$ followed by measuring the ancilla qubit. The multiple-qumode trial ansatz state can be implemented by augmenting the SNAP-displacement ansatz with a two-qumode beam splitter gate

$$BS_{j,k}(\beta, \phi) = e^{i\beta/2(e^{i\phi} \hat{b}_j^\dagger \hat{b}_k + \text{h.c.})} \quad (39)$$

since universality for one qumode combined with beam splitter implies multimode universality.^{46,49} Specifically, the multimode trial state can then be written as

$$|\psi\rangle = U_A^{(D)}(\mathbf{v}) |0_1, \dots, 0_{N_R}\rangle \quad (40a)$$

$$U_A^{(D)}(\mathbf{v}) = U_{\text{BSD}}(\boldsymbol{\theta}^{(D)}, \phi^{(D)}, \beta^{(D)}, \phi^{(D)}) \dots U_{\text{BSD}}(\boldsymbol{\theta}^{(1)}, \phi^{(1)}, \beta^{(1)}, \phi^{(1)}) \quad (40b)$$

$$U_{\text{BSD}} = \left[\prod_{1 \leq j < k \leq N_R} BS_{j,k}(\beta_{j,k}, \phi_{j,k}) \right] \left[\prod_{j=1}^{N_R} S_j(\theta_j) D_j(\alpha_j) \right] \quad (40c)$$

where the subscripts j, k represent qumodes, \mathbf{v} represents all the parameters, and D is the trial ansatz circuit depth.

We will now discuss the implementation of the universal ansatz on near-term qubit-qumode devices. As mentioned above, an ancilla transmon qubit is assumed for implementing all the qumode gates such as SNAP, whereas the controlled-SNAP gates for each of the qumodes can be implemented following Figure 9. Indeed, a tunable beam splitter between two qumodes in the cQED formalism can be realized by coupling the resonator qumodes to a bichromatically driven superconducting transmon,^{59,60} although it can also be implemented by connecting the resonators with a superconducting coupler.^{61,62} The full circuit is illustrated in Figure 12, where it is assumed that one transmon qubit is helping implement all one-qumode SNAP or displacement gates and two-qumode beam splitter gates where all the other qumodes are assumed to be unaffected. In reality, this approach can lead to *crosstalk* among the qumodes in the strongly dispersive regime where the SNAP-displacement ansatz is implemented.⁴⁶ A straightforward way to avoid the crosstalk would be to have separate ancilla transmon qubits for each of the qumodes. Even though this approach will need as many qubits as the qumodes, the qubits are only used for implementing qumode gates. There has been a pioneering development in ref 58 which avoids crosstalk in qumodes by

realizing efficient switching of the qubit-qumode interaction regimes without impacting the resonators. The authors in ref 58 achieve this by combining a standard resonator coupled to a superconducting quantum interference device (SQUID)-based transmon with a cleverly designed magnetic hose.⁶³ The magnetic hose is a cylinder consisting of concentric aluminum and mu-metal layers and is placed perpendicular to the SQUID coax line, as illustrated in Figure 13.

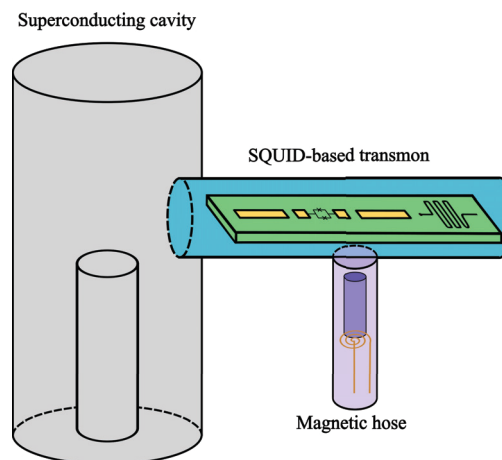


Figure 13. Qubit-qumode hardware that can efficiently switch between different interaction regimes, as described in ref 58. The microwave resonator is coupled to a superconducting quantum interference device (SQUID)-based transmon, which is connected to a magnetic hose made from aluminum and mu-metal layers.

We also discuss an alternative approach below, where the ancilla transmon qubit is connected only to two *primary* qumodes whereas the other qumode gates are implemented using qumode-SWAP gates. The two-qumode SWAP gates can be implemented as $BS(\pi, \pi/2)$,^{25,64} which means that beam splitter interactions are needed between the primary and the other qumodes for this approach. As mentioned above, the beam splitter between two resonators without an ancilla transmon qubit can be achieved by implementing a superconducting coupler between them, such as a superconducting nonlinear asymmetric inductive element (SNAIL)⁶⁵ as demonstrated in ref 62. We illustrate the qumode SWAP and beam splitter gates in Figure 14. Then the multimode trial ansatz as defined in eq (40) can now be implemented using SNAP and displacement gates on the primary qumodes combined with SWAP gates with other qumodes, as illustrated in Figure 15. Similarly, the controlled unitaries on the Hadamard test can also be implemented on the primary

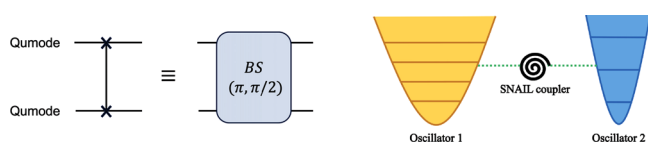


Figure 14. Left: Illustration of how a two-qumode SWAP gate can be implemented by a beam splitter. Right: Illustration of realization of beam splitter of two microwave resonator qumodes without an ancilla transmon by coupling them with a superconducting nonlinear asymmetric inductive element (SNAIL) device.

qumodes with SWAP gates, as illustrated in Figure 16. This approach is also resource-adaptive since more than two primary qumodes can be chosen by introducing additional ancilla transmon qubits based on the connectivity of the couplers connecting the primary qumodes to other qumodes.

We apply our multimode approach to the ground states for the dissociation of linear H_4 molecule, where all the H–H bonds are assumed the same. Although this is a simple system with four electrons and eight spin–orbitals in a minimal basis, it is known to be a challenging problem when the molecule dissociates giving rise to strongly correlated electronic systems.⁶⁶ Indeed, the classical gold-standard electronic structure methods such as traditional coupled cluster completely fail to describe the dissociation curves of hydrogen chains, making it a family of benchmark problems for strong electron correlation.⁶⁷ After the JWT mapping, the qubit Hamiltonian for the H_4 molecule in STO-3G basis can be represented in the form of Eq. 6 with $N_H = 185$ Pauli word terms. Each of the resulting eight-qubit Pauli words is then mapped to two qumodes. Thus, each of the qumode represented four qubits with a Fock cutoff $L = 16$. We compare our multimode SNAP-VQE for the H_4 molecule with qubit-based VQE based on the unitary coupled cluster with singles and doubles (UCCSD) in Figure 17.³ The SNAP-VQE was implemented using QuTip and OpenFermion with the BFGS optimizer as implemented using TensorFlow,⁶⁸ whereas UCCSD-VQE was implemented using Qiskit with a limited memory variant of the BFGS optimizer.⁶⁹ The trial states for SNAP-VQE with $D = 20$ blocks provide highly accurate ground state energies compared to the exact energies even

when the molecule dissociates. The depth for the qubit-based UCCSD scales as $O(N^2 N_Q^3)$, where N is the number of electrons and N_Q is the number of qubits. It is clear from the right panel of Figure 17 that in the strong correlation regime for H_4 , the SNAP-VQE approach outperforms the qubit-based UCCSD-VQE energy errors which stay barely close to the chemical accuracy range.

5. DISCUSSION

We have introduced a general scheme for mapping the molecular electronic structure Hamiltonian in terms of unitary operations native to bosonic quantum devices such as in the cQED architecture involving microwave resonators coupled with transmon qubits with the help of fermion to qubit mapping such as the Jordan–Wigner transformation. Our work opens the door for simulating molecular electronic structure, and by extension, any many-fermion or many-qubit system, on bosonic quantum devices that use qumodes as the building blocks of quantum information.

After mapping the fermionic Hamiltonian to a qumode Hamiltonian, one can consider the electronic structure of interest as a bosonic problem and apply a bosonic ansatz as the trial state for variationally finding the ground state using a classical-quantum hybrid approach. This is related to the qubit coupled cluster approach, where a hardware-efficient qubit ansatz is used after mapping the electronic structure Hamiltonian to a qubit Hamiltonian.⁷⁰ We have shown how to compute the expectation values using a hybrid quantum device involving one qumode coupled with up to two ancilla qubits. We have also discussed two different hybrid qubit-qumode universal ansatzes that efficiently reproduce the exact energies for the potential energy surface of the H_2 molecule. The SNAP-VQE approach is shown to be more robust than the ECD-VQE from the perspective of mapping the qubit Hamiltonian. It is possible to numerically map a Pauli word to SNAP-displacement gates with manageable circuit depth, whereas the ECD-rotation needs a linear combination of unitary approach to make the circuit depth practical.

The robustness of the SNAP-VQE approach inspired us to generalize the qubit to qumode mapping to multiple qumodes.

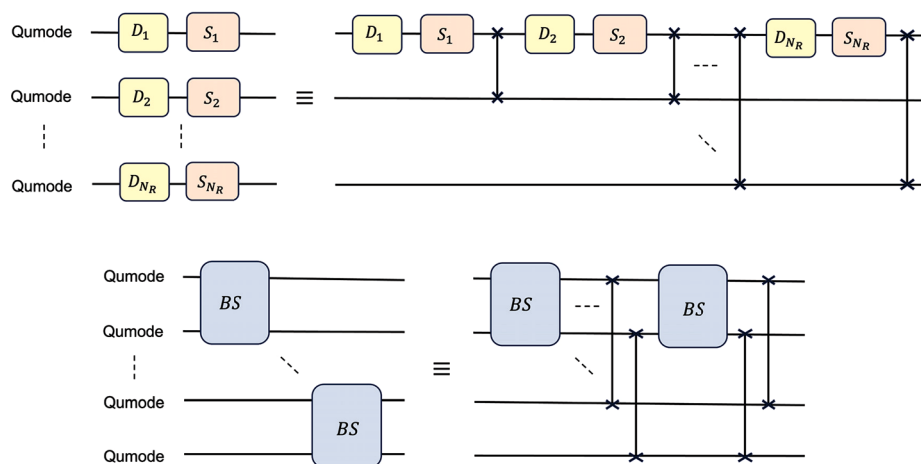


Figure 15. A crosstalk-resistant implementation of multi-qumode trial ansatz circuit originally illustrated in Figure 12. The qumode SWAP gates make sure that all the other gates are implemented using the first two qumodes which are coupled to an ancilla transmon qubit not shown here. The qumode SWAP gates between the first two and the rest of the qumodes can be realized by a superconducting coupler, as illustrated in Figure 14.

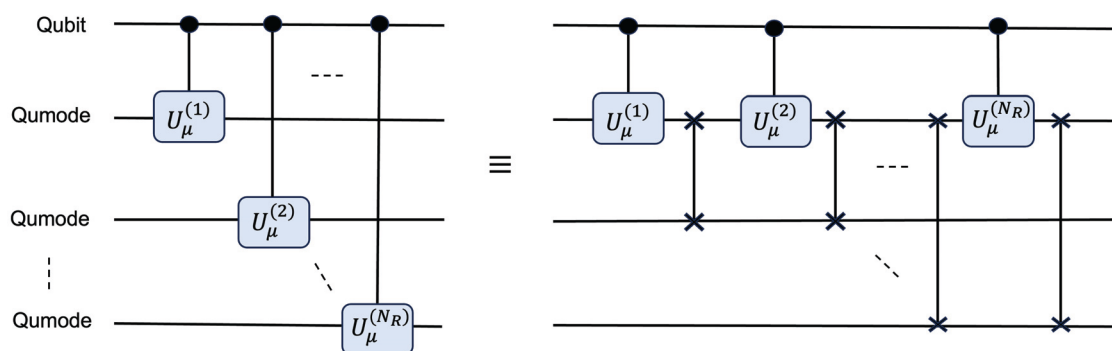


Figure 16. A crosstalk-resistant implementation of part of the circuit corresponding to the multi-qumode Hadamard test originally discussed in Figure 12. The qumode SWAP gates make sure that all the other gates are implemented using the first qumode which is coupled to an ancilla transmon qubit not shown here. The qumode SWAP gates between the first two and the rest of the qumodes can be realized by a superconducting coupler, as illustrated in Figure 14.

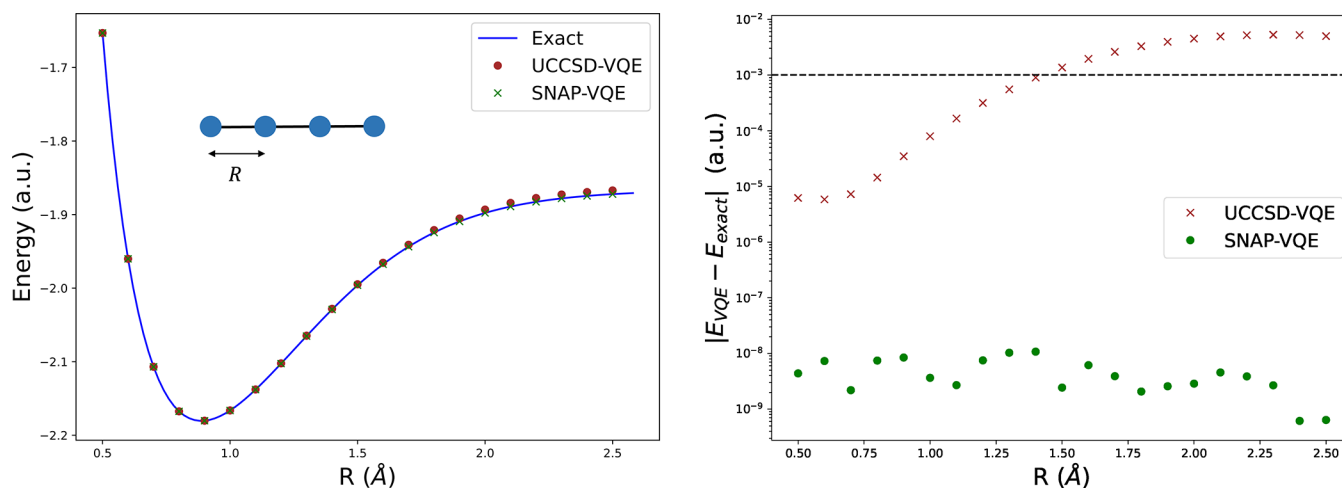


Figure 17. Comparison of linear H_4 molecule ground state energies in STO-3G minimal basis using qubit-based UCCSD-VQE and qumode-based SNAP-VQE approach discussed in Section 4.2. All the H–H bond distances are assumed to be the same and plotted on the horizontal axis. The multimode ansatz circuit for the SNAP-VQE has a depth of $D = 20$ for the trial state preparation part. The black horizontal line in the right panel represents the minimum energy error needed for chemical accuracy, usually in the milliHartree range.

We have introduced a modular approach to partition an arbitrary number of qubits into a few subsystems, each mapped to the Fock basis of a qumode. We have shown that the expectation values can be computed by a sequence of qubit-controlled one-qumode gates followed by measurements in the ancilla qubit. This allowed us to introduce a multi-qumode universal circuit as the trial state ansatz. The universality for the multi-qumode ansatz is achieved by combining the SNAP-displacement gates with two-qumode beam splitter interactions. We have proposed three hardware-efficient approaches to tackle crosstalk constraints between multiple qumodes: using one ancilla transmon qubit per qumode, adapting recent progress on SQUID-based transmons, and employing qumode-SWAP gates to minimize the qubit-qumode connectivity required for high-fidelity operations.

We have applied our multi-qumode SNAP-VQE approach to the linear H_4 , a benchmark molecular electronic system that shows strong electron correlation when all three H–H bonds are stretched. We have numerically demonstrated that the SNAP-VQE approach can provide highly accurate ground state energies for the linear H_4 molecule with two qumodes coupled to one qubit instead of eight qubits in a qubit-centric approach, with a manageable number of qumode gates. We concluded by comparing our method with the benchmark qubit-based

UCCSD-VQE method with a noiseless simulator, which suggests that our approach has the potential to outperform the traditional qubit-based variational approaches for molecular electronic structure in terms of fewer quantum resources and circuit depth. An important aspect of the qumode gates we have explored here would be understanding their optimization landscape for VQE,⁴⁹ which we leave for future development. We remark that the circuits for the two examples presented in our work (H_2 molecule and linear H_4 chain) are shallow such that the intrinsic noisiness of quantum computers, especially photon loss in the qumode resonators, is less significant. We leave the exploration of the effects of noise on our qumode approaches to future work.

APPENDIX A: DIRECT MAPPING FROM FERMIONS TO BOSONS

We will assume real-valued molecular orbitals from now on which leads to the following relations between electron integral tensor elements

$$h_q^p = h_p^q \quad (41a)$$

$$v_{rs}^{pq} = v_{qs}^{pr} = v_{rp}^{sq} = v_{qp}^{sr} \quad (41b)$$

in addition to $v_{rs}^{pq} = v_{sr}^{qp}$ due to the indistinguishability of electrons. It is then possible to write H_{elec} in an alternate form

$$H_{\text{elec}} = \left[\frac{1}{2} \sum_p h_p^p f_p^\dagger f_p + \sum_{p>q} \left(h_q^p f_p^\dagger f_q + \frac{1}{2} \tau_{pq}^{pq} f_p^\dagger f_q f_p f_q \right) \right. \\ \left. + \sum_{p>q>r} \left(\tau_{pr}^{pq} f_p^\dagger f_q f_r + \tau_{qr}^{pq} f_p^\dagger f_q f_r + \tau_{qr}^{pr} f_p^\dagger f_q f_r \right) \right. \\ \left. + \sum_{p>q>r>s} \left(\tau_{rs}^{pq} f_p^\dagger f_q f_r f_s + \tau_{qs}^{pr} f_p^\dagger f_q f_r f_s + \tau_{qr}^{ps} f_p^\dagger f_q f_r f_s \right) \right] + \text{h.c.} \quad (42)$$

where we have defined $\tau_{rs}^{pq} \equiv v_{rs}^{pq} - v_{sr}^{qp}$ such that

$$\tau_{rs}^{pq} = \tau_{rs}^{qp} = -\tau_{sr}^{pq} = \tau_{pq}^{rs} \quad (43)$$

and h.c. represents the Hermitian conjugate of its preceding operator term.

Each term of the electronic Hamiltonian in Eq. 42 has creation and annihilation operators in pairs, which reflects the fact that H_{elec} is number-conserving. Let us define the bilinear fermionic operators⁴²

$$E_q^p \equiv f_p^\dagger f_q = (E_p^q)^\dagger \quad (44)$$

which is equivalent to the number operator when $p = q$ and generalized singles excitation otherwise.⁷¹ A set of $\{E_q^p\}$ can be successively applied to transform between any two Slater determinants with the same number of electrons. The bilinear fermionic operators follow a simple commutation relation

$$[E_q^p, E_s^r] = \delta_{qr} E_s^p - \delta_{ps} E_q^r \quad (45)$$

and generate the $u(M)$ Lie algebra,⁷² where M is the number of spin orbitals. Thus, we can rewrite the electronic Hamiltonian as

$$H_{\text{elec}} = \left[\frac{1}{2} \sum_p h_p^p E_p^p + \sum_{p>q} \left(h_q^p E_q^p + \frac{1}{2} \tau_{qp}^{pq} E_p^p E_q^q \right) \right. \\ \left. + \sum_{p>q>r} \left(\tau_{rp}^{pq} E_p^p E_r^r + \tau_{qr}^{pq} E_q^q E_r^r + \tau_{qr}^{pr} E_p^p E_r^r \right) \right. \\ \left. + \sum_{p>q>r>s} \left(\tau_{sr}^{pq} E_p^p E_r^r E_s^s + \tau_{sq}^{pr} E_p^p E_r^r E_s^s + \tau_{qr}^{ps} E_p^p E_r^r E_s^s \right) \right] + \text{h.c.} \quad (46)$$

where we have applied the adjoint relation for the bilinear fermionic operators and the relations in Eq. 43. Thus, we have written Eq. 46 in such a way that the knowledge about the bilinear fermionic operators $\{E_q^p\}$ with $p \geq q$ is sufficient to represent H_{elec} .

Our goal is to map Eq. 4 to a bosonic state and Eq. 1 to a bosonic Hamiltonian, so that the molecular electronic structure problem can be tackled with bosonic quantum computers. The key results for the direct mapping are given below.

- A system with N fermions can be mapped to a system of N quantum harmonic oscillators (QHOs) or bosonic modes with a maximum of $M - N + 1$ oscillator levels for each.
- An exact injective state mapping exists between Slater determinants and Fock states of QHOs.
- An exact mapping exists between $\{E_q^p\}$ and Fock state projection operators of QHOs.

State Mapping

Elementary bosonic operators follow the canonical commutation relation (CCR)

$$[\hat{b}_p, \hat{b}_q] = \hat{b}_p \hat{b}_q^\dagger - \hat{b}_q \hat{b}_p^\dagger = 0 \quad (47a)$$

$$[\hat{b}_p, \hat{b}_q^\dagger] = \hat{b}_p \hat{b}_q^\dagger - \hat{b}_q^\dagger \hat{b}_p = \delta_{pq} \quad (47b)$$

where \hat{b}_p^\dagger and \hat{b}_p are the bosonic creation and annihilation operators. These operators are defined such that their action on the Fock state $\{|q\rangle | 0 \leq q \leq \infty\}$ of a single qumode is

$$\hat{b}^\dagger |q\rangle_B \equiv \sqrt{q+1} |q+1\rangle_B \quad (48a)$$

$$\hat{b} |q\rangle_B \equiv \sqrt{q} |q-1\rangle_B, \quad q > 0 \quad (48b)$$

$$\hat{b} |0\rangle_B \equiv 0 \quad (48c)$$

which can be trivially generalized to multimodal bosonic systems by taking tensor products of single-mode Fock states. Similar to the fermionic case, the bosonic mode indices in Eq. (47) represent an orthogonal one-particle basis. Each of the bosonic or QHO mode can have infinite levels or occupancies since there is no nilpotency in the CCR. Thus, we define a Fock state of N QHOs as

$$|q_1, \dots, q_N\rangle_B \equiv \frac{(\hat{b}_1^\dagger)^{q_1} \dots (\hat{b}_N^\dagger)^{q_N}}{\sqrt{q_1! \dots q_N!}} |0, \dots, 0\rangle_B \quad (49)$$

where $|0, \dots, 0\rangle_B$ is the ground state of the N oscillators. It should be noted that we only require a bosonic Fock basis of Eq. 49 for this paper, and our approach is agnostic of the properties of the underlying oscillators such as their anharmonicity.

The indices in Eq. 49 represent occupied levels of each mode, in contrast to Eq. 4 where the occupied modes themselves are indexed. This distinction between Eq. 4 and Eq. 49 is simply the result of Pauli exclusion principle and how we have chosen the index ordering in Eq. 4. For example, the bosonic states $|2, 2\rangle_B$, $|2, 3\rangle_B$, $|3, 2\rangle_B$, and $|3, 3\rangle_B$ are all legitimate bosonic states involving the second and third levels of two bosonic modes, whereas $|2, 3\rangle_F$ is the only legitimate fermionic state involving the second and third spin-orbitals. Note that $|2, 3\rangle_F = f_2^\dagger f_3^\dagger |-\rangle_F = -f_3^\dagger f_2^\dagger |-\rangle_F$ respects the permutation of its underlying operators and the resulting sign change, which is similarly true for any Slater determinant defined in Eq. 4.

An injective state mapping exists between Slater determinants of N fermions defined in Eq. 4 and state of N QHOs defined in Eq. 49^{37,73}

$$|p_1, \dots, p_N\rangle_F \leftrightarrow |q_1, \dots, q_N\rangle_B \quad (50)$$

where the relation between the two sets of indices are

$$q_j = p_1 \quad \text{if } j = N \quad (51a)$$

$$= p_{N-j+1} - p_{N-j} - 1 \quad \text{otherwise} \quad (51b)$$

We refer the reader to the [Supplementary Information](#) for a justification of the state mapping. Clearly, the Fermi vacuum $|0, \dots, N-1\rangle_F$ maps to the Fock ground state $|0, \dots, 0\rangle_B$ following Eq. (51). Then the physical interpretation of Eq. 50 is that the holes created from the Fermi vacuum and their impact on it

are regarded as bosonic excitations, as in photoelectron spectroscopy. A schematic for an example state mapping of a system with $N = 4$ electrons is shown in Figure 18.

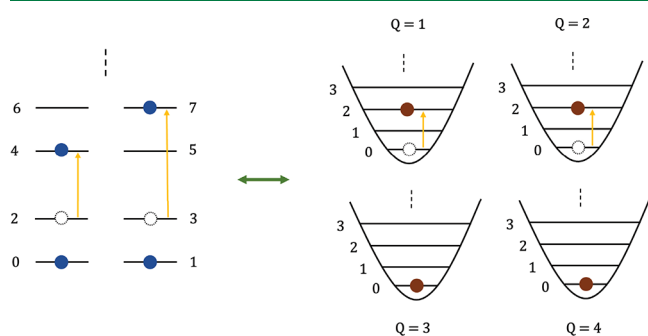


Figure 18. State diagrams corresponding to the state mapping as defined in Eq. 50 and eq (51). Here, a system with $N = 4$ electrons is mapped to a system of four quantum harmonic oscillators. In the initial state, the Slater determinant $|0, 1, 2, 3\rangle_F$ corresponds to four electrons occupying the lowest four spin-orbitals, which is mapped to the oscillator vacuum state $|0, 0, 0, 0\rangle_B$. When some of the occupied spin-orbitals are now excited to get the Slater determinant $|0, 1, 4, 7\rangle_F$, it gets mapped to the Fock state $|2, 2, 0, 0\rangle_B$. The occupied spin-orbitals for electrons and excitation levels for oscillators are represented by blue and brown circles, respectively.

It is thus possible to apply the state mapping of Eq. 50 to map the full configuration interaction (FCI) state for an N -fermion system as

$$|\Psi\rangle = \sum_{1 \leq p_1 < \dots < p_N \leq M} C_{p_1 \dots p_N} |p_1, \dots, p_N\rangle_F \rightarrow \sum_{1 \leq q_1 < \dots < q_N \leq M} C_{q_1 \dots q_N} |q_1, \dots, q_N\rangle_B \quad (52)$$

where the scalars $\{C_{p_1 \dots p_N}\}$ are the FCI coefficients and the $\{q_j\}$ indices are defined in Eq. (51). Since any N -fermion state can be represented as a special case of FCI, Eq. 52 allows mapping any state corresponding to a fermionic system with a fixed particle number to a bosonic state with the number of modes same as the number of fermions. Based on Eq. (51), it is easy to see that the highest integer corresponding to the indices $\{q_j\}$ in Eq. 52 is $L = M - N$. Thus, the state mapping naturally truncates the dimension of the Fock basis, i.e., number of qumode levels, based on the M number of spin-orbitals for a given electronic system, which makes the relevant bosonic Hilbert space isomorphic to the Hilbert space of N qudits⁷⁴ of $M - N + 1$ dimension.

As a specific example, let us discuss the state mapping of Eq. 50 for a system with $N = 2$ with arbitrary $M > 2$ number of spin-orbitals. Mapping between an arbitrary Slater determinant

$$|p, q\rangle_F \equiv f_p^\dagger f_q^\dagger |-\rangle \quad (53)$$

and the mapped state of two qumodes

$$|j, k\rangle_B \equiv \frac{1}{\sqrt{j!k!}} (\hat{b}_1^\dagger)^j (\hat{b}_2^\dagger)^k |0, 0\rangle_B \quad (54)$$

is given by the following relations

$$p = k, \quad j = q - p - 1, \quad q = j + k + 1 \quad (55)$$

For example, if $M = 4$, then the transformations are

$$|0, 1\rangle_F \leftrightarrow |0, 0\rangle_B, \quad |0, 2\rangle_F \leftrightarrow |1, 0\rangle_B, \quad |0, 3\rangle_F \leftrightarrow |2, 0\rangle_B \quad (56a)$$

$$|1, 2\rangle_F \leftrightarrow |0, 1\rangle_B, \quad |1, 3\rangle_F \leftrightarrow |1, 1\rangle_B, \quad |2, 3\rangle_F \leftrightarrow |0, 2\rangle_B \quad (56b)$$

We have so far focused on mapping a Slater determinant into a multimodal bosonic state, but as evident from Eq. 50, the reverse is also true. For example, we write the bosonic states that did not appear in Eq. (56) but still correspond to two harmonic oscillator modes with three levels below

$$|1, 2\rangle_B \leftrightarrow |2, 4\rangle_F, \quad |2, 1\rangle_B \leftrightarrow |1, 4\rangle_F, \quad |2, 2\rangle_B \leftrightarrow |2, 5\rangle_F \quad (57)$$

which are mapped to a Slater determinants of a $N = 2$ system that have $M > 4$ spin-orbitals.

Operator Mapping

The Dhar–Mandal–Suryanarayana (DMS) transformation maps $\{E_p^p\}$ operators into Fock state projection operators of QHOs.³⁸ The DMS transformation was derived from the state mapping of Eq. 50 in ref 38. We simply state the resulting expressions of the DMS transformation here and refer the reader to the [Supplementary Information](#) for more insight into its derivation.

Let us define the bosonic Fock space projection operator corresponding to a given set of k harmonic oscillator modes as

$$\mathcal{P}_{r_1, \dots, r_k} \equiv |r_1, \dots, r_k\rangle\langle r_1, \dots, r_k| \quad (58)$$

and similarly define a related operator as

$$C_{k,a} = \sum_{\substack{r_1 + \dots + r_k \\ = a}} \mathcal{P}_{r_1, \dots, r_k} \quad (59)$$

where each index $\{r_j | 0 \leq r_j \leq L\}$ has a specific range based on the highest physical mode level that needs to be accessed following the state mapping. The expectation value of the operator in Eq. 59 can be computed from the same set of photon number measurements. Let us also denote the identity operator acting on the first k harmonic oscillator modes as

$$\mathcal{I}_k \equiv \mathbb{1}_1 \otimes \dots \otimes \mathbb{1}_k \quad (60)$$

Then the DMS mapping for any number operator E_p^p is

$$E_p^p \rightarrow \mathcal{I}_{N-1} \otimes |p\rangle\langle p| + \sum_{k=1}^{N-1} \mathcal{I}_{k-1} \otimes C_{N-k+1, p-N+k} \quad (61)$$

where $0 \leq p \leq M - 1$. Thus, there is N number of operator terms in Eq. 61 of the form defined in Eq. 59. Operator terms involving more than one number operators can be similarly expressed and simplified due to the projection operator in Eq. 61.

Let us now define the *normalized* bosonic creation and annihilation operators

$$\sigma^\dagger |q\rangle_B \equiv |q + 1\rangle_B \quad (62a)$$

$$\sigma |q\rangle_B \equiv |q - 1\rangle_B, \quad q > 0 \quad (62b)$$

$$\sigma |0\rangle_B \equiv 0 \quad (62c)$$

which can easily be extended for multimodal systems. The DMS mapping expression for the $p > q$ case consists of Fock projection operators as in Eq. 61 with the $\{\sigma_k^\dagger, \sigma_k\}$ operators. We show an example of the generalized singles excitation mapping with $q = p + 1$ below

$$E_q^{q+1} \rightarrow \sigma_1^\dagger C_{N,q-N+1} + \sum_{k=1}^{N-1} \mathcal{I}_{k-1} \otimes \sum_a \sigma_k \mathcal{P}_{q+a} \otimes \sigma_{k+1}^\dagger C_{N-k,q-N+k+1} \quad (63)$$

and state the general expression for the mapping of $\{E_q^p\}$ operators in the [Supplementary Information](#).

As a specific example, let us discuss the DMS operator mapping for the specific case of $N = 2$ with an arbitrary $M > 2$ number of spin-orbitals. The number operators can be mapped as

$$E_p^p \rightarrow \mathbb{1} \otimes |p\rangle\langle p| + \sum_{j+k=p-1} |j, k\rangle\langle j, k| \quad (64)$$

where $p = 0, 1, \dots, M - 1$. The off-diagonal fermionic bilinear operators can be mapped as

$$E_q^{q+p} \rightarrow (\sigma_1^\dagger)^p \sum_{j+k=q-1} |j, k\rangle\langle j, k| + \sigma_1^p (\sigma_2^\dagger)^p \sum_j |j+p, q\rangle\langle j+p, q| - \sum_{j=0}^{p-2} (\sigma_1^\dagger)^{p-2-j} \sigma_1^j (\sigma_2^\dagger)^{j+1} |j, q\rangle\langle j, q| \quad (65)$$

where $q = 0, 1, \dots, M - 1$ and $p = 1, 2, \dots, M - q - 1$. It is also possible to have an alternate representation of the DMS mapping for the $N = 2$ case by applying Eq. (62)

$$E_p^p \rightarrow \mathbb{1} \otimes |p\rangle\langle p| + \sum_{j+k=p-1} |j, k\rangle\langle j, k| \quad (66a)$$

$$E_q^{q+p} \rightarrow \sum_{j+k=q-1} |j+p, k\rangle\langle j, k| + \sum_j |j, q+p\rangle\langle j+p, q| - \sum_{j=0}^{p-2} |p-2-j, q+j+1\rangle\langle j, q| \quad (66b)$$

We mention two examples of mapping the number operators below

$$E_0^0 \rightarrow \mathbb{1} \otimes |0\rangle\langle 0| \quad (67a)$$

$$E_1^1 \rightarrow \mathbb{1} \otimes |1\rangle\langle 1| + |0\rangle\langle 0, 0| \quad (67b)$$

Similarly, the off-diagonal bilinear fermionic operators can be mapped, with two examples given below

$$E_0^1 \rightarrow \sum_{j=1}^L |j-1, 1\rangle\langle j, 0| \quad (68a)$$

$$E_0^2 \rightarrow \left(\sum_{j=1}^{L-1} |j-1, 2\rangle\langle j+1, 0| \right) - |0, 1\rangle\langle 0, 0| \quad (68b)$$

where we truncated the expansion based on the highest relevant level of the bosonic modes. We refer the reader to the [Supplementary Information](#) for applying the direct mapping to the electronic structure Hamiltonian of the dihydrogen molecule in a minimal basis.

■ APPENDIX B: MATRIX REPRESENTATION OF BOSONIC OPERATORS

We review the finite matrix representation of bosonic operators in the Fock basis, where the matrix dimensions are $L \times L$ with L being the Fock cutoff chosen for the qumode. For a bosonic operator O , the matrix elements are given by $O_{n,m} = \langle n|O|m\rangle$, where $\{|n\rangle\}$ are the Fock basis states. The matrices for the bosonic creation and annihilation operators are

$$\hat{b} = \begin{pmatrix} 0 & 0 & 0 & \cdots & 0 \\ \sqrt{1} & 0 & 0 & \cdots & 0 \\ 0 & \sqrt{2} & 0 & \cdots & 0 \\ \vdots & \vdots & \vdots & \ddots & \vdots \\ 0 & 0 & 0 & \cdots & \sqrt{L-1} \end{pmatrix} \quad (69a)$$

$$\hat{b}^\dagger = \begin{pmatrix} 0 & \sqrt{1} & 0 & \cdots & 0 \\ 0 & 0 & \sqrt{2} & \cdots & 0 \\ 0 & 0 & 0 & \ddots & 0 \\ \vdots & \vdots & \vdots & \ddots & \sqrt{L-1} \\ 0 & 0 & 0 & \cdots & 0 \end{pmatrix} \quad (69b)$$

The matrix form for the bosonic number operator is simply

$$\hat{n} = \begin{pmatrix} 0 & 0 & 0 & \cdots & 0 \\ 0 & 1 & 0 & \cdots & 0 \\ 0 & 0 & 2 & \cdots & 0 \\ \vdots & \vdots & \vdots & \ddots & \vdots \\ 0 & 0 & 0 & \cdots & L-1 \end{pmatrix} \quad (70)$$

Thus, any qumode operator can now be represented with $L \times L$ matrices by using matrix multiplications involving eq (69) and Eq. 70.

■ APPENDIX C: ECD WITH QUBIT ROTATION

Alternate Forms

The position and momentum operators of the qumode are

$$\hat{q} = \frac{1}{\sqrt{2}}(\hat{b}^\dagger + \hat{b}) \quad (71a)$$

$$\hat{p} = \frac{i}{\sqrt{2}}(\hat{b}^\dagger - \hat{b}) \quad (71b)$$

where we assumed atomic units. The displacement operator can now be written as

$$D(\beta) = e^{\beta \hat{b}^\dagger - \beta^* \hat{b}} = e^{i\sqrt{2}[\text{Im}(\beta)\hat{q} - \text{Re}(\beta)\hat{p}]} \quad (72)$$

The conditional displacement operator is defined as

$$CD(\beta) = e^{iZ \otimes (\beta \hat{b}^\dagger - \beta^* \hat{b})} = e^{iZ \otimes \sqrt{2}[\text{Im}(\beta)\hat{q} - \text{Re}(\beta)\hat{p}]} = e^{iZ \otimes \mathcal{A}(\beta)} \quad (73)$$

where $\mathcal{A}(\beta) = -\mathcal{A}(-\beta)$. We now Taylor expand Eq. 73 to get

$$\begin{aligned} CD(\beta) &= \mathbb{1} \otimes \left[\mathbb{1} + \frac{i^2}{2!} \mathcal{A}^2(\beta) + \dots \right] \\ &\quad + Z \otimes \left[i\mathcal{A}(\beta) + \frac{i^3}{3!} \mathcal{A}^3(\beta) + \dots \right] \\ &= (|0\rangle\langle 0| + |1\rangle\langle 1|) \otimes \left[\mathbb{1} + \frac{i^2}{2!} \mathcal{A}^2(\beta) + \dots \right] \\ &\quad + (|0\rangle\langle 0| - |1\rangle\langle 1|) \otimes \left[i\mathcal{A}(\beta) + \frac{i^3}{3!} \mathcal{A}^3(\beta) \right. \\ &\quad \left. + \dots \right] \end{aligned} \quad (74)$$

where we have used the relation $Z^2 = \mathbb{I}$. We now rearrange Eq. 74 to arrive at an alternate form of the conditional displacement operator

$$CD(\beta) = |0\rangle\langle 0| \otimes D(\beta) + |1\rangle\langle 1| \otimes D(-\beta) \quad (75)$$

Thus the ECD operator is related to the conditional displacement as

$$ECD(\beta) = (\sigma_x \otimes \mathbb{I})CD(\beta/2) = |1\rangle\langle 0| \otimes D(\beta/2) + |0\rangle\langle 1| \otimes D(-\beta/2) \quad (76)$$

The ECD with qubit rotation operator $U_{ER}(\beta, \theta, \varphi) = ECD(\beta)[R(\theta, \varphi) \otimes \mathbb{I}]$ can be written in a block matrix form as^{45,60}

$$U_{ER}(\beta, \theta, \varphi) = \begin{bmatrix} e^{i(\varphi-\pi/2)\sin(\theta/2)\mathbf{D}(-\beta/2)} & \cos(\theta/2)\mathbf{D}(-\beta/2) \\ \cos(\theta/2)\mathbf{D}(\beta/2) & -e^{-i(\varphi-\pi/2)\sin(\theta/2)\mathbf{D}(\beta/2)} \end{bmatrix} \quad (77)$$

where the qubit rotation $R(\theta, \varphi) = \exp[-i(\theta/2)(\cos \varphi \sigma_x + \sin \varphi \sigma_y)]$ is generated by the σ_x and σ_y Pauli matrices. Here, $\mathbf{D}(\beta)$ in Eq. 77 represents the $L \times L$ matrix representation of the displacement operator following Appendix B, where L is Fock cutoff chosen for the qumode.

Universality

A Hamiltonian H is called a generator of the corresponding unitary $U = e^{iH}$. The set of ECD gates and qubit rotations has shown to be universal since linear combinations of repeated nested commutators of the elementary set generators cover the full Lie algebra corresponding to the combined space of a qubit-qumode system.^{45,60} Let us review the justification here. Given a set of generating Hamiltonians A and B , the following relations are true^{75,76}

$$e^{\delta t^2[A, B]} = e^{-i\delta t A} e^{-i\delta t B} e^{i\delta t A} e^{i\delta t B} + O(\delta t^3) \quad (78a)$$

$$e^{\delta t(A+B)} = e^{i\delta t/2A} e^{i\delta t/2B} e^{i\delta t/2B} e^{i\delta t/2A} + O(\delta t^3) \quad (78b)$$

which can be applied to generate the unitary corresponding to the Hamiltonians $-i[A, B]$ and $A+B$ in the $\delta t \rightarrow 0$ limit. By the repeated application of Eq. (78), it is possible to generate unitaries corresponding to the linear combination of the nested commutators of the original set of generators. Thus, universality for a qubit-qumode system means the ability to implement any unitary transformation that can be generated from an arbitrary linear combination of Hamiltonians of the form $\sigma_i \hat{q}^j \hat{p}^k$, where j, k are non-negative integers and $\sigma_i \in \{\mathbb{I}_2, \sigma_x, \sigma_y, \sigma_z\}$ is one of the Pauli matrices.

As discussed in Section C.1, the generators of ECD with qubit rotation are $\{\sigma_z \hat{q}, \sigma_x \hat{p}, \sigma_x, \sigma_y\}$. We will now show how to expand this generator set using commutators to achieve universality. First, we apply the following commutators

$$\begin{aligned} [\sigma_z \hat{q}, \sigma_x] &= 2i\sigma_z \hat{q}, & [\sigma_z \hat{q}, \sigma_y] &= -2i\sigma_z \hat{q}, & [\sigma_x \hat{p}, \sigma_x] &= 2i\sigma_x \hat{p}, \\ [\sigma_x \hat{p}, \sigma_y] &= -2i\sigma_x \hat{p} \end{aligned} \quad (79)$$

to include the generators $\{\sigma_a \hat{q}, \sigma_a \hat{p}\}$ with $a \in \{x, y, z\}$. Repeated applications of the following commutators

$$[\sigma_x \hat{q}, \sigma_y \hat{q}] = 2i\sigma_x \hat{q}^2, \quad [\sigma_y \hat{q}, \sigma_z \hat{q}] = 2i\sigma_y \hat{q}^2, \quad [\sigma_z \hat{q}, \sigma_x \hat{q}] = 2i\sigma_z \hat{q}^2 \quad (80a)$$

$$[\sigma_x \hat{p}, \sigma_y \hat{p}] = 2i\sigma_x \hat{p}^2, \quad [\sigma_y \hat{p}, \sigma_z \hat{p}] = 2i\sigma_y \hat{p}^2, \quad [\sigma_z \hat{p}, \sigma_x \hat{p}] = 2i\sigma_z \hat{p}^2 \quad (80b)$$

$$[\sigma_y \hat{q}, \sigma_z \hat{q}^2] = 2i\sigma_y \hat{q}^3, \quad [\sigma_z \hat{q}, \sigma_x \hat{q}^2] = 2i\sigma_z \hat{q}^3, \quad [\sigma_x \hat{q}, \sigma_y \hat{q}^2] = 2i\sigma_x \hat{q}^3 \quad (80c)$$

$$[\sigma_x \hat{p}, \sigma_y \hat{p}^2] = 2i\sigma_x \hat{p}^3, \quad [\sigma_y \hat{p}, \sigma_z \hat{p}^2] = 2i\sigma_y \hat{p}^3, \quad [\sigma_z \hat{p}, \sigma_x \hat{p}^2] = 2i\sigma_z \hat{p}^3 \quad (80d)$$

⋮

include generators $\sigma_a \hat{q}^j$ with $j \geq 2$. Similarly, by repeated application of the following commutators

$$[\sigma_x \hat{q}^{j+1}, \sigma_y \hat{p}] = 2i\sigma_x \hat{p} \hat{q}^{j+1} + (j+1)i\sigma_x \sigma_y \hat{q}^j \quad (81a)$$

$$[\sigma_y \hat{q}^{j+1}, \sigma_z \hat{p}] = 2i\sigma_y \hat{p} \hat{q}^{j+1} + (j+1)i\sigma_y \sigma_z \hat{q}^j \quad (81b)$$

$$[\sigma_z \hat{q}^{j+1}, \sigma_x \hat{p}] = 2i\sigma_z \hat{p} \hat{q}^{j+1} + (j+1)i\sigma_z \sigma_x \hat{q}^j \quad (81c)$$

$$[\sigma_x \hat{p} \hat{q}^{j+1}, \sigma_y \hat{p}] = 2i\sigma_x \hat{p}^2 \hat{q}^{j+1} + (j+1)i\sigma_x \sigma_y \hat{p} \hat{q}^j \quad (81d)$$

$$[\sigma_y \hat{p} \hat{q}^{j+1}, \sigma_z \hat{p}] = 2i\sigma_y \hat{p}^2 \hat{q}^{j+1} + (j+1)i\sigma_y \sigma_z \hat{p} \hat{q}^j \quad (81e)$$

$$[\sigma_z \hat{p} \hat{q}^{j+1}, \sigma_x \hat{p}] = 2i\sigma_z \hat{p}^2 \hat{q}^{j+1} + (j+1)i\sigma_z \sigma_x \hat{p} \hat{q}^j \quad (81f)$$

⋮

we have covered all polynomial terms $\sigma_c \hat{q}^j \hat{p}^k$ with $c \in \{x, y, z\}$, which has sufficient for universality for the composite qubit-qumode system, where we have used the relation $[\hat{q}^{j+1}, \hat{p}] = (j+1)i\hat{q}^j$. The universality for only the qumode can be shown by using the commutator

$$[\sigma_x \hat{p}^j \hat{q}^{k+1}, \sigma_x \hat{p}] = i(k+1)\hat{p}^j \hat{q}^k \quad (82)$$

which eliminates the Pauli operators. It should be noted that this proof does not specify how many blocks of ECD gate with qubit rotation can reproduce an arbitrary qubit-qumode unitary or an arbitrary qumode unitary.

■ APPENDIX D: SNAP-DISPLACEMENT ANSATZ

The SNAP gate defined in Eq. 32 allows the application of different phases on each Fock basis state of a qumode and can also be equivalently defined as

$$S(\theta) = \exp\left(i \sum_{n=0}^{L-1} \theta_n |n\rangle\langle n|\right) \quad (83)$$

where L is the Fock cutoff chosen for the qumode. Although conceptually understood as a qumode operator, realistically the SNAP gate is implemented via strongly dispersive qubit-cavity interactions in which the ancillary qubit is rotated whenever the cavity has n photons, consecutively for each n between 0 and $L-1$.⁷⁷ Since the qubit remains in $|0\rangle$ after the SNAP operation,⁴⁷ it can also be written as

$$S(\theta) = |0\rangle\langle 0| \otimes \exp\left(i \sum_{n=0}^{L-1} \theta_n |n\rangle\langle n|\right) + |1\rangle\langle 1| \otimes \mathbb{I} \quad (84)$$

Equivalently, it can also be represented by the following qubit-qumode operator²⁵

$$S(\theta) = \exp\left(iZ \otimes \sum_{n=0}^{L-1} \theta_n |n\rangle\langle n|\right) \quad (85)$$

We note that the exact energies for the potential energy surface for the H_2 can be obtained by the Hadamard test as

shown in Figure 8, where each layer of the controlled-(SNAP-displacement) ansatz can be decomposed as a controlled-SNAP and controlled-displacement. Similar to Appendix C.2, to prove the universality of the SNAP with displacement ansatz, as defined in Eq. 33, we focus on its initial generator set. The generators for the displacement operator $D(\alpha)$ with real-valued α is \hat{p} and the generator for SNAP operator is

$$Q_n = \sum_{n'=0}^n |n'\rangle\langle n'| \quad (86)$$

The commutator of the initial generator set

$$J_n = i[\hat{p}, Q_n] = \sqrt{n+1}(|n\rangle\langle n+1| + \text{h.c.}) \quad (87)$$

can selectively couple the basis states $|n\rangle$ and $|n-1\rangle$. Thus, for any integer $L > 0$, the operators $\{J_n\}_{n=0}^{L-1}$ and $\{Q_n\}_{n=0}^{L-1}$ are sufficient to generate the Lie algebra $u(L)$ over the truncated Fock space, which implies universal oscillator control.⁴⁷

APPENDIX E: HARDWARE IMPLEMENTATION OF UNIVERSAL BOSONIC GATES

Decomposition of Controlled-ECD Operation

We provide here an explicit, hardware-efficient compilation of the controlled-ECD (cECD) operation, defined as a qubit (a) controlling the native dispersive interaction between a bosonic mode (b) and its auxiliary qubit:

$$\begin{aligned} c_a \text{ECD}_b(\beta) &= |0_a\rangle\langle 0_a| \otimes \mathbb{I}_b + |1_a\rangle \\ &\langle 1_a| \otimes \frac{|1_b\rangle\langle 0_b| \otimes D_b(\beta/2) + |0_b\rangle\langle 1_b| \otimes D_b(-\beta/2)}{\text{ECD}_b(\beta) \text{ as defined in Eq. (11)}} \end{aligned} \quad (88)$$

Here, we assume native access to qubit–qubit CNOT operations and conditional displacement (CD) gates. Apart from previous demonstration in the strong dispersive limit,⁷⁸ Eq. 76 suggests that the CD gate is also implementable in the weakly dispersive regime with one native ECD operation and one bit-flip

$$CD_b(\beta/2) = (X_b \otimes \mathbb{I}_b) \text{ECD}_b(\beta) \quad (89)$$

We now show analytically that the compiled circuit as shown in Figure 19 holds. Indeed,

$$\begin{aligned} &CD_b\left(\frac{-\beta}{4}\right) (c_a X_b) CD_b\left(\frac{\beta}{4}\right) \\ &= [\mathbb{I}_a \otimes (|0_b\rangle\langle 0_b| \otimes D(-\beta/4) + |1_b\rangle\langle 1_b| \otimes D(\beta/4))] \\ &\quad (c_a X_b) \\ &\times [\mathbb{I}_a \otimes (|0_b\rangle\langle 0_b| \otimes D(\beta/4) + |1_b\rangle\langle 1_b| \otimes D(-\beta/4))] \\ &= [\mathbb{I}_a \otimes (|0_b\rangle\langle 0_b| \otimes D(-\beta/4) + |1_b\rangle\langle 1_b| \otimes D(\beta/4))] \\ &\times [|0_a\rangle\langle 0_a| \otimes (|0_b\rangle\langle 0_b| \otimes D(\beta/4) + |1_b\rangle\langle 1_b| \otimes D(-\beta/4)) + \\ &|1_a\rangle\langle 1_a| \otimes (|1_b\rangle\langle 0_b| \otimes D(\beta/4) + |0_b\rangle\langle 1_b| \otimes D(-\beta/4))] \\ &= |0_a\rangle\langle 0_a| \otimes \mathbb{I}_b + |1_a\rangle\langle 1_a| \otimes [|1_b\rangle\langle 0_b| \otimes D(\beta/2) + |0_b\rangle\langle 1_b| \\ &\quad \otimes D(-\beta/2)] \\ &= c_a \text{ECD}_b(\beta) \end{aligned} \quad (90)$$

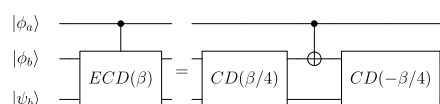


Figure 19. Compiled circuit for controlled-ECD operation using native gates. $|\psi_b\rangle$ and its corresponding wire represents a qumode whereas the other wires represent ancilla qubits.

Comparison of ECD-Rotation and SNAP-Displacement Gates

Both the ECD with qubit rotation and SNAP with displacement gates are implemented at the hardware by tuning the dynamics of an oscillator qumode with an ancilla qubit. The Hamiltonian of the qubit-qumode system for the SNAP gate is⁴⁷

$$\hat{H} = \hat{H}_0 + \hat{H}_1 + \hat{H}_2 \quad (91)$$

Here, \hat{H}_0 represents a dispersively coupled qubit and cavity oscillator

$$\hat{H}_0 = \omega_q |e\rangle\langle e| + \omega_c \hat{n} - \chi |e\rangle\langle e| \hat{n} \quad (92)$$

where ω_q is the transition frequency between the qubit states $|g\rangle$ and $|e\rangle$, ω_c is the oscillator frequency, $\hat{n} = \hat{b}^\dagger \hat{b}$ is the number operator of the qumode, and χ is the dispersive coupling. The Hamiltonian \hat{H}_1 represents the time-dependence of the oscillator

$$\hat{H}_1 = \epsilon(t) e^{i\omega_q t} \hat{b}^\dagger + \text{h.c.} \quad (93)$$

with the oscillator drive denoted by $\epsilon(t)$. The Hamiltonian \hat{H}_2 represents the time-dependence of the qubit

$$\hat{H}_1 = \Omega(t) e^{i\omega_q t} |e\rangle\langle g| + \text{h.c.} \quad (94)$$

with the qubit drive denoted by $\Omega(t)$. The control scheme for the SNAP gate requires that $|\Omega(t)| \ll \chi$, i.e., the qubit drive is weak compared with the dispersive coupling.⁴⁷ In contrast, the ECD gate is implemented in the weak dispersive regime, where $\chi \leq \max(\Gamma_1, \Gamma_2, \kappa)$, where Γ_1, Γ_2 are qubit decoherence and relaxation rates, and κ is the oscillator relaxation rate.⁴⁵ In other words, the SNAP operation is only natively available in the strong dispersive region, whereas the ECD operation only operates in the weak dispersive region and involves unselective ancilla control which allows higher resiliency against crosstalk.⁴⁶ A mixed hardware architecture comprising both SNAP and ECD gates could potentially be enabled by a programmable, fast beam splitter with a three-wave mixing coupler,⁶² which remains an exciting future direction.

ASSOCIATED CONTENT

Data Availability Statement

The Python code and data for the ansatz optimization, state preparation simulations and figure generation can be found at https://github.com/CQDMQD/qumode_est_paper.

Supporting Information

The Supporting Information is available free of charge at <https://pubs.acs.org/doi/10.1021/acs.jctc.4c01400>.

Additional theoretical details including overview of the electronic structure problem, justification and derivation of the DMS operator mapping, bosonic Hamiltonian for the H_2 molecule alongside illustrations of the parametric dependence of its coefficients (Figure S1), heatmap of

the Hamiltonian matrix elements (Figure S2), cQED-based subspace tomography for photon transfer expectation values, hybrid variational approach with the universal bosonic ansatz for two qumodes and one ancilla qubit (Figure S3), and comparison of ground state energies of H₂ molecule with various approaches (Figure S4) (PDF)

AUTHOR INFORMATION

Corresponding Author

Victor S. Batista – Department of Chemistry, Yale University, New Haven, Connecticut 06520, United States; Yale Quantum Institute, Yale University, New Haven, Connecticut 06511, United States; orcid.org/0000-0002-3262-1237; Email: victor.batista@yale.edu

Authors

Rishab Dutta – Department of Chemistry, Yale University, New Haven, Connecticut 06520, United States; orcid.org/0000-0001-7675-1431

Nam P. Vu – Department of Chemistry, Yale University, New Haven, Connecticut 06520, United States; Department of Chemistry, Lafayette College, Easton, Pennsylvania 18042, United States; Department of Electrical and Computer Engineering, Lafayette College, Easton, Pennsylvania 18042, United States; orcid.org/0000-0002-3849-5139

Chuzhi Xu – Department of Chemistry, Yale University, New Haven, Connecticut 06520, United States; orcid.org/0009-0003-6622-4752

Delmar G. A. Cabral – Department of Chemistry, Yale University, New Haven, Connecticut 06520, United States; orcid.org/0009-0001-1195-5529

Ningyi Lyu – Department of Chemistry, Yale University, New Haven, Connecticut 06520, United States; orcid.org/0000-0001-9239-9925

Alexander V. Soudackov – Department of Chemistry, Yale University, New Haven, Connecticut 06520, United States; orcid.org/0000-0001-9581-8494

Xiaohan Dan – Department of Chemistry, Yale University, New Haven, Connecticut 06520, United States; orcid.org/0000-0001-8069-1101

Haote Li – Department of Chemistry, Yale University, New Haven, Connecticut 06520, United States; orcid.org/0000-0002-8146-5066

Chen Wang – Department of Physics, University of Massachusetts—Amherst, Amherst, Massachusetts 01003, United States

Complete contact information is available at: <https://pubs.acs.org/10.1021/acs.jctc.4c01400>

Notes

The authors declare no competing financial interest.

ACKNOWLEDGMENTS

We acknowledge support from the NSF for the Center for Quantum Dynamics on Modular Quantum Devices (CQD-MQD) under grant number CHE-2124511. R.D. thanks Brandon Allen and Francesco Calcagno for useful discussions. N.P.V. acknowledges support from the Lafayette College Bergh Family Fellows Program.

REFERENCES

- (1) Vogiatzis, K. D.; Ma, D.; Olsen, J.; Gagliardi, L.; De Jong, W. A. Pushing configuration-interaction to the limit: Towards massively parallel MCSCF calculations. *J. Chem. Phys.* **2017**, *147*, 184111.
- (2) Chan, G. K.-L. Spiers Memorial Lecture: Quantum chemistry, classical heuristics, and quantum advantage. *Faraday Discuss.* **2024**, *254*, 11–52.
- (3) Peruzzo, A.; McClean, J.; Shadbolt, P.; Yung, M.-H.; Zhou, X.-Q.; Love, P. J.; Aspuru-Guzik, A.; O'Brien, J. L. A Variational Eigenvalue Solver on a Photonic Quantum Processor. *Nat. Commun.* **2014**, *5*, 4213.
- (4) Grimsley, H. R.; Economou, S. E.; Barnes, E.; Mayhall, N. J. An adaptive variational algorithm for exact molecular simulations on a quantum computer. *Nat. Commun.* **2019**, *10*, 3007.
- (5) McArdle, S.; Jones, T.; Endo, S.; Li, Y.; Benjamin, S. C.; Yuan, X. Variational ansatz-based quantum simulation of imaginary time evolution. *npj Quantum Inf.* **2019**, *5*, 75.
- (6) Motta, M.; Sun, C.; Tan, A. T.; O'Rourke, M. J.; Ye, E.; Minnich, A. J.; Brandao, F. G.; Chan, G. K.-L. Determining eigenstates and thermal states on a quantum computer using quantum imaginary time evolution. *Nat. Phys.* **2020**, *16*, 205.
- (7) Smart, S. E.; Mazziotti, D. A. Quantum solver of contracted eigenvalue equations for scalable molecular simulations on quantum computing devices. *Phys. Rev. Lett.* **2021**, *126*, 070504.
- (8) Kyaw, T. H.; Soley, M. B.; Allen, B.; Bergold, P.; Sun, C.; Batista, V. S.; Aspuru-Guzik, A. Boosting quantum amplitude exponentially in variational quantum algorithms. *Quantum Sci. Technol.* **2024**, *9*, 01LT01.
- (9) Whitfield, J. D.; Biamonte, J.; Aspuru-Guzik, A. Simulation of electronic structure Hamiltonians using quantum computers. *Mol. Phys.* **2011**, *109*, 735.
- (10) Seeley, J. T.; Richard, M. J.; Love, P. J. The Bravyi-Kitaev transformation for Quantum Computation of Electronic Structure. *J. Chem. Phys.* **2012**, *137*, 224109.
- (11) Dutta, R.; Cabral, D. G.; Lyu, N.; Vu, N. P.; Wang, Y.; Allen, B.; Dan, X.; Cortiñas, R. G.; Khazaei, P.; Smart, S. E. Simulating Chemistry on Bosonic Quantum Devices. *J. Chem. Theory Comput.* **2024**, *20*, 6426.
- (12) Huh, J.; Guerreschi, G.; Peropadre, B.; McClean, J. R.; Aspuru-Guzik, A. Boson sampling for molecular vibronic spectra. *Nat. Photonics* **2015**, *9*, 615.
- (13) Wang, C. S.; Curtis, J. C.; Lester, B. J.; Zhang, Y.; Gao, Y. Y.; Freeze, J.; Batista, V. S.; Vaccaro, P. H.; Chuang, I. L.; Frunzio, L.; Jiang, L.; Girvin, S. M.; Schoelkopf, R. J. Efficient Multiphoton Sampling of Molecular Vibronic Spectra on a Superconducting Bosonic Processor. *Phys. Rev. X* **2020**, *10*, 021060.
- (14) Malpathak, S.; Kallullathil, S. D.; Izmaylov, A. F. Simulating Vibrational Dynamics on Bosonic Quantum Devices. *J. Phys. Chem. Lett.* **2025**, *16*, 1855.
- (15) Wang, C. S.; Frattini, N. E.; Chapman, B. J.; Puri, S.; Girvin, S. M.; Devoret, M. H.; Schoelkopf, R. J. Observation of wave-packet branching through an engineered conical intersection. *Phys. Rev. X* **2023**, *13*, 011008.
- (16) Lyu, N.; Miano, A.; Tsioutsios, I.; Cortiñas, R. G.; Jung, K.; Wang, Y.; Hu, Z.; Geva, E.; Kais, S.; Batista, V. S. Mapping Molecular Hamiltonians into Hamiltonians of Modular cQED Processors. *J. Chem. Theory Comput.* **2023**, *19*, 6564.
- (17) Cabral, D. G. A.; Khazaei, P.; Allen, B. C.; Videla, P. E.; Schäfer, M.; Cortiñas, R. G.; Carrillo de Albornoz, A. C.; Chávez-Carlos, J.; Santos, L. F.; Geva, E. A Roadmap for Simulating Chemical Dynamics on a Parametrically Driven Bosonic Quantum Device. *J. Phys. Chem. Lett.* **2024**, *15*, 12042–12050.
- (18) Copetudo, A.; Fontaine, C. Y.; Valadares, F.; Gao, Y. Y. Shaping photons: Quantum information processing with bosonic cQED. *Appl. Phys. Lett.* **2024**, *124*, 080502.
- (19) Deleglise, S.; Dotsenko, I.; Sayrin, C.; Bernu, J.; Brune, M.; Raimond, J.-M.; Haroche, S. Reconstruction of non-classical cavity field states with snapshots of their decoherence. *Nature* **2008**, *455*, 510.

- (20) Hacker, B.; Welte, S.; Daiss, S.; Shaikat, A.; Ritter, S.; Li, L.; Remppe, G. Deterministic creation of entangled atom–light Schrödinger-cat states. *Nat. Photonics* **2019**, *13*, 110.
- (21) Bruzewicz, C. D.; Chiaverini, J.; McConnell, R.; Sage, J. M. Trapped-ion quantum computing: Progress and challenges. *Appl. Phys. Rev.* **2019**, *6*, 021314.
- (22) Araz, J. Y.; Grau, M.; Montgomery, J.; Ringer, F. Toward hybrid quantum simulations with qubits and qumodes on trapped-ion platforms. *arXiv preprint arXiv:2410.07346* 2024, DOI: 10.48550/arXiv.2410.07346.
- (23) Joshi, A.; Noh, K.; Gao, Y. Y. Quantum information processing with bosonic qubits in circuit QED. *Quantum Sci. Technol.* **2021**, *6*, 033001.
- (24) Blais, A.; Grimsmo, A. L.; Girvin, S. M.; Wallraff, A. Circuit quantum electrodynamics. *Rev. Mod. Phys.* **2021**, *93*, 025005.
- (25) Liu, Y.; Singh, S.; Smith, K. C.; Crane, E.; Martyn, J. M.; Eickbusch, A.; Schuckert, A.; Li, R. D.; Sinanan-Singh, J.; Soley, M. B.; Hybrid oscillator-qubit quantum processors: Instruction set architectures, abstract machine models, and applications. *arXiv preprint arXiv:2407.10381* 2024, DOI: 10.48550/arXiv.2407.10381.
- (26) Crane, E.; Smith, K. C.; Tomesh, T.; Eickbusch, A.; Martyn, J. M.; Kühn, S.; Funcke, L.; DeMarco, M. A.; Chuang, I. L.; Wiebe, N.; Hybrid Oscillator-Qubit Quantum Processors: Simulating Fermions, Bosons, and Gauge Fields. *arXiv preprint arXiv:2409.03747* 2024, DOI: 10.48550/arXiv.2409.03747.
- (27) Romanenko, A.; Pilipenko, R.; Zorzetti, S.; Frolov, D.; Awida, M.; Belomestnykh, S.; Posen, S.; Grassellino, A. Three-Dimensional Superconducting Resonators at $T < 20$ mK with Photon Lifetimes up to $\tau = 2$ s. *Phys. Rev. Appl.* **2020**, *13*, 034032.
- (28) Ring, P.; Schuck, P. *The Nuclear Many-Body Problem*; Springer-Verlag, 1980.
- (29) Garbaczewski, P. Representations of the CAR Generated by Representations of the CCR. Fock Case. *Commun. Math. Phys.* **1975**, *43*, 131.
- (30) Garbaczewski, P. The method of Boson expansions in quantum theory. *Phys. Rep.* **1978**, *36*, 65.
- (31) Klein, A.; Marshalek, E. Boson realizations of Lie algebras with applications to nuclear physics. *Rev. Mod. Phys.* **1991**, *63*, 375.
- (32) Ginocchio, J. N.; Johnson, C. W. Fermion to boson mappings revisited. *Phys. Rep.* **1996**, *264*, 153.
- (33) Von Delft, J.; Schoeller, H. Bosonization for beginners—re-fermionization for experts. *Ann. Phys.* **1998**, *510*, 225.
- (34) Scuseria, G. E.; Henderson, T. M.; Bulik, I. W. Particle-particle and quasiparticle random phase approximations: Connections to coupled cluster theory. *J. Chem. Phys.* **2013**, *139*, 104113.
- (35) Liu, J. A unified theoretical framework for mapping models for the multi-state Hamiltonian. *J. Chem. Phys.* **2016**, *145*, 204105.
- (36) Montoya-Castillo, A.; Markland, T. E. On the exact continuous mapping of fermions. *Sci. Rep.* **2018**, *8*, 12929.
- (37) Ohta, K. New bosonic excitation operators in many-electron wave functions. *Int. J. Quantum Chem.* **1998**, *67*, 71.
- (38) Dhar, A.; Mandal, G.; Suryanarayana, N. V. Exact operator bosonization of finite number of fermions in one space dimension. *J. High Energy Phys.* **2006**, *2006*, 118.
- (39) Qin, M.; Schäfer, T.; Andergassen, S.; Corboz, P.; Gull, E. The Hubbard model: A computational perspective. *Annu. Rev. Condens. Matter Phys.* **2022**, *13*, 275.
- (40) Szabo, A.; Ostlund, N. S. *Modern Quantum Chemistry*; Dover Publications, 1996.
- (41) Helgaker, T.; Jørgensen, P.; Olsen, J. *Molecular Electronic Structure Theory*; John Wiley and Sons, 2000.
- (42) Jordan, P. Der Zusammenhang der symmetrischen und linearen Gruppen und das Mehrkörperproblem. *Zeitschrift für Physik* **1935**, *94*, 531.
- (43) Liu, Y.; Che, S.; Zhou, J.; Shi, Y.; Li, G. Fermihedral: On the Optimal Compilation for Fermion-to-Qubit Encoding. *Proceedings of the 29th ACM International Conference on Architectural Support for Programming Languages and Operating Systems* **2024**, *3*, 382–397.
- (44) Babbush, R.; Wiebe, N.; McClean, J.; McClain, J.; Neven, H.; Chan, G. K.-L. Low-Depth Quantum Simulation of Materials. *Phys. Rev. X* **2018**, *8*, 011044.
- (45) Eickbusch, A.; Sivak, V.; Ding, A. Z.; Elder, S. S.; Jha, S. R.; Venkatraman, J.; Royer, B.; Girvin, S. M.; Schoelkopf, R. J.; Devoret, M. H. Fast universal control of an oscillator with weak dispersive coupling to a qubit. *Nat. Phys.* **2022**, *18*, 1464.
- (46) You, X.; Lu, Y.; Kim, T.; Kurkcuoglu, D. M.; Zhu, S.; van Zanten, D.; Roy, T.; Lu, Y.; Chakram, S.; Grassellino, A.; Romanenko, A.; Koch, J.; Zorzetti, S. Crosstalk-Robust Quantum Control in Multimode Bosonic Systems. *Phys. Rev. Appl.* **2024**, *22*, 044072.
- (47) Krastanov, S.; Albert, V. V.; Shen, C.; Zou, C.-L.; Heeres, R. W.; Vlastakis, B.; Schoelkopf, R. J.; Jiang, L. Universal control of an oscillator with dispersive coupling to a qubit. *Phys. Rev. A* **2015**, *92*, 040303.
- (48) Diringer, A. A.; Blumenthal, E.; Grinberg, A.; Jiang, L.; Hacohe-Gourgy, S. Conditional-not Displacement: Fast Multi-oscillator Control with a Single Qubit. *Phys. Rev. X* **2024**, *14*, 011055.
- (49) Zhang, B.; Zhuang, Q. Energy-dependent barren plateau in bosonic variational quantum circuits. *Quantum Sci. Technol.* **2025**, *10*, 015009.
- (50) Job, J. Efficient, direct compilation of SU(N) operations into SNAP & Displacement gates. *arXiv preprint arXiv:2307.11900* 2023, DOI: 10.48550/arXiv.2307.11900.
- (51) Shang, Z.-X.; Zhong, H.-S.; Zhang, Y.-K.; Yu, C.-C.; Yuan, X.; Lu, C.-Y.; Pan, J.-W.; Chen, M.-C. Boson sampling enhanced quantum chemistry. *arXiv preprint arXiv:2403.16698* 2024, DOI: 10.48550/arXiv.2403.16698.
- (52) Ryabinkin, I. G.; Genin, S. N.; Izmaylov, A. F. Constrained variational quantum eigensolver: Quantum computer search engine in the Fock space. *J. Chem. Theory Comput.* **2019**, *15*, 249.
- (53) Hehre, W. J.; Stewart, R. F.; Pople, J. A. Self-consistent molecular-orbital methods. I Use of Gaussian expansions of Slater-type atomic orbitals. *J. Chem. Phys.* **1969**, *51*, 2657.
- (54) Virtanen, P.; Gommers, R.; Oliphant, T. E.; Haberland, M.; Reddy, T.; Cournapeau, D.; Burovski, E.; Peterson, P.; Weckesser, W.; Bright, J.; van der Walt, S. J.; Brett, M.; Wilson, J.; Millman, K. J.; Mayorov, N.; Nelson, A. R. J.; Jones, E.; Kern, R.; Larson, E.; Carey, C. J.; Polat, I.; Feng, Y.; Moore, E. W.; VanderPlas, J.; Laxalde, D.; Perktold, J.; Cimrman, R.; Henriksen, I.; Quintero, E. A.; Harris, C. R.; Archibald, A. M.; Ribeiro, A. H.; Pedregosa, F.; van Mulbregt, P. SciPy 1.0: Fundamental Algorithms for Scientific Computing in Python. *Nat. Methods* **2020**, *17*, 261–272.
- (55) Lambert, N.; Giguère, E.; Menczel, P.; Li, B.; Hopf, P.; Suárez, G.; Gali, M.; Lishman, J.; Gadhvi, R.; Agarwal, R.; QuTiP 5: The Quantum Toolbox in Python. *arXiv preprint arXiv:2412.04705* 2024, DOI: 10.48550/arXiv.2412.04705.
- (56) McClean, J. R.; Sung, K.; Kivlichan, I.; Cao, Y.; Dai, C.; Fried, E.; Gidney, C.; Gimby, B.; Gokhale, P.; Häner, T.; Openfermion: The electronic structure package for quantum computers. *eprint arXiv:1710.07629* 2017, DOI: 10.48550/arXiv.1710.07629.
- (57) Fösel, T.; Krastanov, S.; Marquardt, F.; Jiang, L. Efficient cavity control with SNAP gates. *arXiv preprint arXiv:2004.14256* 2020, DOI: 10.48550/arXiv.2004.14256.
- (58) Valadares, F.; Huang, N.-N.; Chu, K. T. N.; Dorogov, A.; Chua, W.; Kong, L.; Song, P.; Gao, Y. Y. On-demand transposition across light-matter interaction regimes in bosonic cQED. *Nat. Commun.* **2024**, *15*, 5816.
- (59) Gao, Y. Y.; Lester, B. J.; Zhang, Y.; Wang, C.; Rosenblum, S.; Frunzio, L.; Jiang, L.; Girvin, S. M.; Schoelkopf, R. J. Programmable Interference between Two Microwave Quantum Memories. *Phys. Rev. X* **2018**, *8*, 021073.
- (60) Zhang, Y.; Lester, B. J.; Gao, Y. Y.; Jiang, L.; Schoelkopf, R. J.; Girvin, S. M. Engineering bilinear mode coupling in circuit QED: Theory and experiment. *Phys. Rev. A* **2019**, *99*, 012314.
- (61) Lu, Y.; Maiti, A.; Garmon, J. W.; Ganjam, S.; Zhang, Y.; Claes, J.; Frunzio, L.; Girvin, S. M.; Schoelkopf, R. J. High-fidelity parametric beamsplitting with a parity-protected converter. *Nat. Commun.* **2023**, *14*, 5767.

(62) Chapman, B. J.; de Graaf, S. J.; Xue, S. H.; Zhang, Y.; Teoh, J.; Curtis, J. C.; Tsunoda, T.; Eickbusch, A.; Read, A. P.; Koottandavida, A.; Mundhada, S. O.; Frunzio, L.; Devoret, M.; Girvin, S.; Schoelkopf, R. High-On-Off-Ratio Beam-Splitter Interaction for Gates on Bosonically Encoded Qubits. *PRX Quantum* **2023**, *4*, 020355.

(63) Gargiulo, O.; Oleschko, S.; Prat-Camps, J.; Zanner, M.; Kirchmair, G. Fast flux control of 3D transmon qubits using a magnetic hose. *Appl. Phys. Lett.* **2021**, *118*, 012601.

(64) Fujii, K. Exchange gate on the qudit space and Fock space. *Journal of Optics B: Quantum and Semiclassical Optics* **2003**, *5*, S613.

(65) Frattini, N.; Vool, U.; Shankar, S.; Narla, A.; Sliwa, K.; Devoret, M. 3-wave mixing Josephson dipole element. *Appl. Phys. Lett.* **2017**, *110*, 222603.

(66) Vaquero-Sabater, N.; Carreras, A.; Orús, R.; Mayhall, N. J.; Casanova, D. Physically Motivated Improvements of Variational Quantum Eigensolvers. *J. Chem. Theory Comput.* **2024**, *20*, 5133.

(67) Motta, M.; Ceperley, D. M.; Chan, G. K.-L.; Gomez, J. A.; Gull, E.; Guo, S.; Jiménez-Hoyos, C. A.; Lan, T. N.; Li, J.; Ma, F.; Millis, A. J.; Prokofev, N. V.; Ray, U.; Scuseria, G. E.; Sorella, S.; Stoudenmire, E. M.; Sun, Q.; Tupitsyn, I. S.; White, S. R.; Zgid, D.; Zhang, S. Towards the Solution of the Many-Electron Problem in Real Materials: Equation of State of the Hydrogen Chain with State-of-the-Art Many-Body Methods. *Phys. Rev. X* **2017**, *7*, 031059.

(68) Abadi, M.; Agarwal, A.; Barham, P.; Brevdo, E.; Chen, Z.; Citro, C.; Corrado, G. S.; Davis, A.; Dean, J.; Devin, M.; Ghemawat, S.; Goodfellow, I.; Harp, A.; Irving, G.; Isard, M.; Jia, Y.; Jozefowicz, R.; Kaiser, L.; Kudlur, M.; Levenberg, J.; Mané, D.; Monga, R.; Moore, S.; Murray, D.; Olah, C.; Schuster, M.; Shlens, J.; Steiner, B.; Sutskever, I.; Talwar, K.; Tucker, P.; Vanhoucke, V.; Vasudevan, V.; Viégas, F.; Vinyals, O.; Warden, P.; Wattenberg, M.; Wicke, M.; Yu, Y.; Zheng, X. TensorFlow: Large-Scale Machine Learning on Heterogeneous Systems. 2015; <https://www.tensorflow.org/Software> available from tensorflow.org.

(69) Javadi-Abhari, A.; Treinish, M.; Krsulich, K.; Wood, C. J.; Lishman, J.; Gacon, J.; Martiel, S.; Nation, P. D.; Bishop, L. S.; Cross, A. W.; Quantum computing with Qiskit. *arXiv preprint arXiv:2405.08810* 2024, DOI: 10.48550/arXiv.2405.08810.

(70) Ryabinkin, I. G.; Yen, T.-C.; Genin, S. N.; Izmaylov, A. F. Qubit Coupled Cluster Method: A Systematic Approach to Quantum Chemistry on a Quantum Computer. *J. Chem. Theory Comput.* **2018**, *14*, 6317.

(71) Nakatsuji, H. Structure of the exact wave function. *J. Chem. Phys.* **2000**, *113*, 2949.

(72) Fukutome, H. The Group Theoretical Structure of Fermion Many-Body Systems Arising from the Canonical Anticommutation Relation. I. *Prog. Theor. Phys.* **1981**, *56*, 809.

(73) Suryanarayana, N. V. Half-BPS giants, free fermions and microstates of superstars. *J. High Energy Phys.* **2006**, *2006*, 82.

(74) Wang, Y.; Hu, Z.; Sanders, B. C.; Kais, S. Qudits and high-dimensional quantum computing. *Front. Phys.* **2020**, *8*, 589504.

(75) Lloyd, S.; Braunstein, S. L. Quantum Computation over Continuous Variables. *Phys. Rev. Lett.* **1999**, *82*, 1784.

(76) Braunstein, S. L.; van Loock, P. Quantum information with continuous variables. *Rev. Mod. Phys.* **2005**, *77*, 513.

(77) Heeres, R. W.; Vlastakis, B.; Holland, E.; Krastanov, S.; Albert, V. V.; Frunzio, L.; Jiang, L.; Schoelkopf, R. J. Cavity State Manipulation Using Photon-Number Selective Phase Gates. *Phys. Rev. Lett.* **2015**, *115*, 137002.

(78) Leghtas, Z.; Kirchmair, G.; Vlastakis, B.; Devoret, M. H.; Schoelkopf, R. J.; Mirrahimi, M. Deterministic protocol for mapping a qubit to coherent state superpositions in a cavity. *Phys. Rev. A* **2013**, *87*, 042315.